Geophys. J. Int. (2000) **142,** 000–000

A three dimensional radially anisotropic model of shear velocity in the whole mantle

Mark Panning[1⋆] and Barbara Romanowicz[1]

[1] *Berkeley Seismological Laboratory, University of California, Berkeley, CA* 94720*, USA*

Received 2004 Month Day; in original form 2004 March 5

SUMMARY

We present a degree 24 3D shear velocity model of the whole mantle including radial anisotropy to degree 16 (SAW24AN16), obtained using a large three component surface and body waveform dataset and an iterative inversion for structure and source parameters based on Nonlinear Asymptotic Coupling Theory (NACT) (Li & Romanowicz 1995). The model shows a link between mantle flow and anisotropy in a variety of depth ranges. In the uppermost mantle, we confirm observations of regions with $V_{SH} > V_{SV}$ starting at ∼80 km under oceanic regions and ∼200 km under stable continental lithosphere, suggesting horizontal flow beneath the lithosphere (Gung *et al.* 2003). We also observe a $V_{SV} > V_{SH}$ signature at ∼200-300 km depth beneath major ridge systems with amplitude correlated with spreading rate. In the transition zone (400-700 km depth), regions of subducted slab material are associated with $V_{SV} > V_{SH}$, while the ridge signal decreases except under the East Pacific Rise. While the mid-mantle has lower amplitude anisotropy ($<1\%$), we also confirm the observation of strong radially symmetric $V_{SH} > V_{SV}$ in the lowermost 300 km (Panning & Romanowicz 2004). The 3D deviations from this degree 0 signature are associated with the transition to the large-scale low-velocity superplumes under the central Pacific and Africa, suggesting that $V_{SH} > V_{SV}$ is generated in the predominant horizontal flow of a mechanical boundary layer, with a change in signature related to transition to upwelling at the superplumes. We also solve for source perturbations in an iterative procedure. Source perturbations are generally small compared to

published Harvard CMT solutions, but improve the fit to the data. The sources in the circum-Pacific subduction zones show small but systematic shifts in location.

Key words: radial anisotropy; tomography; upper mantle; transition zone; D”

1 INTRODUCTION

The 3D seismic velocity structure of the Earth’s mantle represents a snapshot of its current thermal and chemical state. As tomographic models of the isotropic seismic velocity converge in their long wavelength features (Masters *et al.* 2000; Gu *et al.* 2001; Grand 1997; Mégnin & Romanowicz 2000; Ritsema & van Heijst 2000), geodynamicists use them to infer the density structure, and thus the buoyancy contrasts which drive mantle convection (Hager 1984; Ricard & Vigny 1989; Woodward *et al.* 1993; Daradich *et al.* 2003). This process, however, is complicated by the difficulty of separating thermal and chemical contrasts, and the lack of direct sensitivity of seismic velocities to the density contrasts which drive the convection.

In many regions of the mantle, analyzing the anisotropy of seismic velocities can give us another type of constraint on mantle dynamics. Nearly all the constituent minerals of the mantle have strongly anisotropic elastic properties on the microscopic scale. Random orientations of these crystals, though, tend to cancel out this anisotropy on the macroscopic scale observable by seismic waves. In general, to produce observable seismic anisotropy, deformation processes need to either align the individual crystals (lattice preferred orientation or LPO) (e.g. Karato (1998a)), or cause alignment of pockets or layers of materials with strongly contrasting elastic properties (shape preferred orientation or SPO) (Kendall & Silver 1996). While in the relatively cold regions of the lithosphere these anisotropic signatures can remain frozen-in over geologic time-scales (Silver 1996), observed anisotropy at greater depths likely requires dynamic support (Vinnik *et al.* 1992). Thus, the anisotropy observed at sub-lithospheric depths is most likely a function of the current mantle strain field, and these observations, coupled with mineral physics observations and

*Author to whom correspondence should be addressed

predictions of the relationship between strain and anisotropy of mantle materials at the proper pressure and temperature conditions, can help us map out mantle flow.

Some of the earliest work on large-scale patterns of anisotropy focussed on the uppermost mantle. Studies showed significant P velocity anisotropy from body wave refraction studies (Hess 1964), as well as S anisotropy from incompatibility between Love and Rayleigh wave dispersion characteristics (e.g. McEvilly (1964)). These observations were supported and extended globally by the inclusion of 1D radial anisotropic structure in the upper 220 km of the global reference model PREM (Dziewonski & Anderson 1981), based on normal mode observations. More recently, much upper mantle work has focussed on the observation of shear-wave splitting, particularly in SKS phases. This approach allows for the detection and modelling of azimuthal anisotropy on fine lateral scales, but there is little depth resolution and there are tradeoffs between the strength of anisotropy and the thickness of the anisotropic layer. These tradeoffs make it very difficult, for example, to distinguish between models with anisotropy frozen in the lithosphere (Silver 1996) or dynamically generated in the deforming mantle at greater depths (Vinnik *et al.* 1992). Shear-wave splitting analysis has also been applied to a variety of phases to look at anisotropy to deeper depths in subduction zones (Fouch & Fischer 1996). Many other studies have observed anisotropy in several geographic regions in the lowermost mantle using phases such as ScS and S_{diff} (e.g. (Lay & Helmberger 1983; Vinnik *et al.* 1989; Kendall & Silver 1996; Matzel *et al.* 1997; Garnero & Lay 1997; Pulliam & Sen 1998; Lay *et al.* 1998; Russell *et al.* 1999)). With observations of anisotropy in many geographical regions and at a variety of depths in the mantle, a global picture of the 3D variation of anisotropy, such as that obtained by tomographic approaches, is desirable.

There has been increasing refinement of global 3D tomographic models of both P and S velocity over the last ten years, using a variety of datasets, including absolute travel times, relative travel times measured by cross-correlation, surface wave phase velocities, free oscillations, and complete body and surface waveforms. While most of these models assume isotropic velocities, a few global anisotropic models have been developed. Best resolved is upper mantle radial and azimuthal anisotropy using fundamental mode surface waves (Tanimoto & Anderson 1985; Nataf *et al.* 1986; Montagner & Tanimoto 1991; Ekström & Dziewonski 1998; Beghein & Trampert 2004)

and recently with the inclusion of overtones (Gung *et al.* 2003) as well as some recent attempts at tomographically mapping transition zone radial (Beghein & Trampert 2003) and azimuthal (Trampert & van Heijst 2002) S anisotropy, radial S anisotropy in D″ (Panning & Romanowicz 2004) and finally P velocity anisotropy in the whole mantle (Boschi & Dziewonski 2000).

In our earlier work, we have developed a complete waveform inversion technique which we used to focus on anisotropic structure in the upper mantle (Gung *et al.* 2003) and the core-mantle boundary region (Panning & Romanowicz 2004). Here we extend this modelling approach to map anisotropy throughout the mantle, and explore the uncertainties and implications of the model.

2 MODELLING APPROACH

2.1 Parameterization

While an isotropic elastic model requires only two independent elastic moduli (e.g. the bulk and shear moduli), a general anisotropic elastic medium is defined by 21 independent elements of the fourth-order elastic stiffness tensor. Attempting to resolve all of these elements independently throughout the mantle is not a reasonable approach, as the data are not capable of resolving so many parameters independently, and physical interpretation of such complicated structure would be far from straight-forward. For this reason, many assumptions of material symmetry can be made to reduce the number of unknowns.

A common assumption is that the material has hexagonal symmetry, which means that the elastic properties are symmetric about an axis (Babuska & Cara 1991). This type of symmetry can be used to approximate, for example, macroscopic samples of deformed olivine (the dominant mineral of the upper mantle) (Kawasaki & Konno 1984). If the symmetry axis is arbitrarily oriented, this type of material can lead to observations of radial anisotropy (with a vertical symmetry axis), as well as azimuthal anisotropy, where velocities depend on the horizontal azimuth of propagation. However, with sufficient azimuthal coverage, the azimuthal variations will be averaged out, and we can instead focus only on the remaining terms related to a radially anisotropic model.

This reduces the number of independent elastic coefficients to 5. These have been traditionally

defined by the Love coefficients: A, C, F, L, and N (Love 1927). These coefficients can be related to observable seismic velocities:

$$A = \rho V_{PH}^2 \tag{1}$$

$$C = \rho V_{PV}^2 \tag{2}$$

$$L = \rho V_{SV}^2 \tag{3}$$

$$N = \rho V_{SH}^2 \tag{4}$$

$$F = \frac{\eta}{(A - 2L)}, \tag{5}$$

where ρ is density, V_{PH} and V_{PV} are the velocities of horizontally and vertically polarized P waves, V_{SH} and V_{SV} are the velocities of horizontally and vertically polarized S waves propagating horizontally, and η is a parameter related to the velocities at angles other than horizontal and vertical. Our dataset of long period waveforms is primarily sensitive to V_{SH} and V_{SV}, so we use empirical scaling parameters (Montagner & Anderson 1989) to further reduce the number of unknowns to 2. Because the partial derivatives with respect to the other anisotropic parameters are small, the particular choice of scaling is not critical.

Although earlier models were developed in terms of V_{SH} and V_{SV} (Gung *et al.* 2003), we choose to parameterize equivalently in terms of Voight average isotropic S and P velocity (Babuska & Cara 1991), and three anisotropic parameters, ξ, ϕ, and η,

$$V_S^2 = \frac{2V_{SV}^2 + V_{SH}^2}{3} \tag{6}$$

$$V_P^2 = \frac{V_{PV}^2 + 4V_{PH}^2}{5} \tag{7}$$

$$\xi = \frac{V_{SH}^2}{V_{SV}^2} \tag{8}$$

$$\phi = \frac{V_{PV}^2}{V_{PH}^2} \tag{9}$$

$$\eta = \frac{F}{(A - 2L)}. \tag{10}$$

We invert for V_S and ξ, and scale V_P and density to V_S, and ϕ and η to ξ, using scaling factors derived from Montagner and Anderson (1989),

$$\frac{\delta \ln V_P}{\delta \ln V_S} = 0.5 \tag{11}$$

$$\frac{\delta \ln \rho}{\delta \ln V_S} = 0.33 \tag{12}$$

$$\frac{\delta \ln \eta}{\delta \ln \xi} = -2.5 \tag{13}$$

$$\frac{\delta \ln \phi}{\delta \ln \xi} = -1.5. \tag{14}$$

This parameterization change is made so as to invert directly for the sense and amplitude of radial anisotropy in S velocity, the quantity of interest. Because damping in the inversion process leads to some degree of uncertainty in the amplitudes and anisotropy is related to the difference between V_{SH} and V_{SV}, inverting for these quantities and then calculating ξ could potentially lead to considerable uncertainty in the amplitude and even the sign of the resolved anisotropy.

The model is parameterized horizontally in terms of spherical harmonics to degree and order 24 for the isotropic velocity and degree and order 16 for the anisotropic parameter ξ, which provides a nominal resolution of features on the order of 1200 km. In depth, the model is parameterized in 16 cubic splines as in Mégnin & Romanowicz (2000). These splines are distributed irregularly in depth, reflecting the irregular distribution of dataset sensitivity with depth, with dense coverage in the uppermost mantle due to the strong sensitivity of surface waves, and also in the core-mantle boundary region, where reflected and diffracted phases have increased sensitivity.

2.2 Theory and dataset

Our approach to tomographic inversion utilizes a dataset of three component long period time-domain ground acceleration seismic waveforms. These waveforms are modelled using non-linear asymptotic coupling theory (NACT) (Li & Romanowicz 1995). NACT is a normal-mode based perturbation approach, which computes coupling between modes both along and across dispersion branches. The asymptotic calculation of this coupling allows us to calculate two dimensional sensitivity kernels along the great circle path between source and receiver. These kernels show both the ray character of phases as well as the sensitivity away from the ray-theoretical paths due to the effect of finite-frequency data (Fig. 1).

In this study, we neglect off-plane focusing effects in the amplitudes, which we feel is reasonable since we reject data that exhibit strong amplitude anomalies, and, most importantly, our algorithm is primarily designed to fit the phase of the waveforms, which is much less affected by off-path effects than the amplitude. We also neglect the effects of azimuthal anisotropy, working from the premise that good azimuthal coverage of our data allows us to retrieve the azimuthally-independent anisotropic signal. There is ample evidence for azimuthal anisotropy in the earth's mantle, and our efforts should be viewed as representing only the first step towards a complete view of global mantle anisotropy.

Expressions for the coupled mode sensitivity kernels used in this approach have been developed for models parameterized in terms of the elastic coefficients A, C, F, L, and N (Li & Romanowicz 1996). The change to the radial anisotropy parameterization described above is accomplished with simple linear combinations of these kernels (Appendix A). Although for fundamental mode surface waves sensitivity is dominated by V_{SH} for transverse component data and by V_{SV} for radial and vertical components, kernels for body waves and overtone surface waves show a much more complex sensitivity along the great-circle path (Fig. 1).

With this approach we are able to use a group velocity windowing scheme (Li & Tanimoto 1993) to efficiently synthesize acceleration wavepackets and calculate partial derivatives with respect to model parameters. Dividing the time-domain waveforms into wavepackets allows a weighting scheme to avoid having larger amplitude phases dominate the inversion. For example, separating fundamental and overtone surface wavepackets allows us to increase the weight of the overtones, increasing sensitivity in the transition zone, while increasing the weight of smaller amplitude phases, such as S_{diff} and multiple ScS, relative to large amplitude upper mantle phases, such as SS, increases our lowermost mantle sensitivity. The final dataset consists of 3 component surface and body wave packets from 1191 events (Table 1). The wavepackets were gathered using an automated picking algorithm described in Appendix B.

To analyze the coverage of our dataset, we calculated the sensitivity kernels for every wavepacket in our dataset. For each wavepacket, we then calculated a root mean squared average over the time dependent sensitivity kernels and applied the weighting values used in our inversion, which ac-

count for waveform amplitude, noise and path redundancy. We then took the values for each great circle path kernel and summed them up in a global grid with blocks 5° by 5° and approximately 200 km in depth. The geographic coverage and depth dependence of sensitivity were then plotted normalized by surface area of each cell (accounting for the smaller cells near the poles) (Fig. 2A-F). Although this system is less intuitive than determining coverage using ray theory and determining ray density in a given cell, it is more applicable to our inversion, because the finite frequency data have sensitivity outside of the infinitesimal ray path and the sensitivity varies along the ray. In order to compare with a ray density approach, given our weighting system, a direct hit (i.e. a ray passing through the center of a cell) contributes $\sim 1 \times 10^{-10}$ to 5×10^{-10} to the cells in Figure 2 (units are s^{-1}, as the kernels represent the modal frequency shift due to a relative perturbation of a model parameter). Phases with ray theoretical paths near a cell, however, can also contribute to the total sensitivity in that cell. The total for each depth range was also summed (Fig. 2G). Fundamental and overtone surface wave sensitivity is very strong in the upper mantle, and sensitivity generally decreases with depth, but note the increase in sensitivity in the lowermost 500 km due to the inclusion of phases such as S_{diff} and multiple ScS. The overall sensitivity to ξ is much lower than the sensitivity to isotropic velocity, but resolution tests indicate we can resolve anisotropic structure in most depth ranges of the mantle (see section 4.1).

The inversion of the dataset is done using an iterative least-squares approach (Tarantola & Valette 1982). This approach includes *a priori* data and model covariance matrices which we can use to apply a data weighting scheme (Li & Romanowicz 1996), as well as constraints on the model norm, and radial and horizontal smoothness. Inversion iterations for anisotropic velocity structure were performed using the source parameters estimated by the Harvard CMT (Centroid Moment Tensor) project (Dziewonski & Woodhouse 1983). The reference model for our inversions is PREM (Dziewonski & Anderson 1981). Because the starting model is important in non-linear iterative inversions, we started from the anisotropic model SAW16AN developed in Gung *et al.*, (2003) to describe the upper mantle. Although this is not a whole mantle model, it was shown to provide a good fit to the surface wave and overtone dataset, as well as to the body wave dataset not sensitive to the core-mantle boundary region. The lower mantle of the starting model is the same

as that of SAW24B16 (Mégnin & Romanowicz 2000), which is a model derived from transverse component only data. We initially inverted for a model parameterized to degree 16 in both isotropic V_S and ξ. After the model reached convergence after three iterations, we iteratively inverted for perturbed source parameters (location, origin time and moment tensor elements) for events with sufficient data (Li & Romanowicz 1996). Holding these parameters fixed, we recalculated the data fit for all wavepackets, adjusted the packet weighting, and inverted for structural parameters again. The model converged in two iterations to a best-fit degree 16 model. We then performed two more iterations with the isotropic V_S parameterized to degree 24 and ξ to degree 16.

While the method remains much less computationally intensive than numerical approaches, the large number of wavepackets gathered (Table 1) can still require heavy computational resources. However, the calculation of the partial derivative matrix, which is the most computationally intensive step, can be very efficiently and naturally parallelized. The partial derivative matrices (multiplied by their respective transpose matrices and the a priori data covariance matrix) for each event can be calculated independently with minimal redundancy, and then combined linearly. Using this approach on a 16 node cluster of dual-processor machines enables us to perform model iterations in a few days, which allows us to ensure convergence as well as analyze subsets of the data to obtain estimates of the statistical error of our models.

3 MODEL RESULTS

3.1 Isotropic velocity model

The isotropic portion of the model (Fig. 3) is quite similar to previous S velocity tomography models. Figure 4 shows the correlation as a function of depth with several recent tomographic models (Ekström & Dziewonski 1998; Gu *et al.* 2001; Ritsema & van Heijst 2000; Masters *et al.* 2000; Mégnin & Romanowicz 2000). The correlations in this figure were calculated by expanding each of the models in spherical harmonics up to degree 24 at the depths of the knots of the radial splines in the parameterization of SAW24AN16. The correlation is then calculated over the set of spherical harmonics coefficients. The correlation is quite good with all models in the uppermost 200 km, but the models diverge somewhat in the transition zone, and more strongly in the

mid-mantle range between 800 and 2000 km depth where amplitudes are low, and are closer in agreement in the lowermost mantle. The correlation is, not surprisingly, strongest with SAW24B16 (Mégnin & Romanowicz 2000), which was the starting model in the lower mantle, as well as being derived from some common transverse component data. SB4L18 (Masters *et al.* 2000) diverges most strongly in the upper mantle, but is actually the best-correlated in the lower mantle, while the two Harvard models, S362D1 (Gu *et al.* 2001) and the isotropic portion of S20A (Ekström & Dziewonski 1998), are the most divergent models in the lowermost mantle. A similar pattern of correlation as a function of depth is seen when any of the other models are compared to the whole set of models, placing the isotropic portion of this model well within the scatter of previously published tomographic models.

The common features of S tomographic models are present in the isotropic velocity model. The uppermost 200 km is dominated by tectonic features, with fast continents and slower oceans that show an age-dependent increase in velocity away from the slow velocities near ridges. Regions of active tectonic processes are, in general, slower, such as western North America, the major circum-Pacific subduction zones, and the East African rift. In the transition zone depth range, the most prominent features are the fast velocities of subducted slabs, while the slow ridges are no longer present. Mid-mantle velocity anomalies are low in amplitude, and more white in spectrum. Finally, in the lowermost 500 km, the amplitudes of heterogeneity increase again, and become dominated by a degree 2 pattern with rings of higher velocities surrounding two lower velocity regions under the central Pacific and Africa, commonly referred to as superplumes.

The first-order control on the fit to the data is the isotropic portion of the model, and this structure is therefore quite stable, whether anisotropy is included in the model or not. Just the isotropic portion of SAW24AN16 leads to a variance reduction of 50.9%, while adding anisotropy improves the variance reduction to 57.0%. While this improvement in fit is certainly significant above the 99% confidence level according to an F-test criterion given the large number of degrees of freedom of our modelling (Menke 1989), the isotropic model is obviously the more important control. To demonstrate the stability of the isotropic structure, we performed an inversion iteration starting from the isotropic portion of the final model, without allowing any anisotropy, aside from

that of the reference model. The resulting isotropic structure is nearly visually indistinguishable, with correlation ranging between 0.92 to above 0.99 as a function of depth with an average of 0.97.

3.2 Upper mantle anisotropy

The ξ structure above 400 km (Fig. 5A,C,E) is similar to that of Gung *et al.* (2003), (hereafter referred to as GPR03) with an average correlation coefficient of 0.71 across this depth range. However, there are some notable differences in the structure when they are compared in detail (Fig. 5). The positive $\delta \ln \xi$ signature under oceans observed previously (Montagner & Tanimoto 1991; Ekström & Dziewonski 1998) continues to greater depths. Although the signature under continental roots discussed in GPR03 still remains in this model, it is slightly lower amplitude and somewhat obscured by the oceanic signature at depth. Despite the differences, the implication of $V_{SH} > V_{SV}$ anisotropy generated in the asthenosphere at different depths beneath the oceanic and continental lithosphere remains.

The differences between this model and the GPR03 model can be explained by the differing vertical resolutions of the two datasets. Although the much greater number of body waves in the current modelling greatly improves coverage in the transition zone and lower mantle, it apparently introduces some vertical smearing in the uppermost mantle. Additionally, the damping scheme chosen for this model was designed to obtain a radially smooth model to avoid potential oscillatory structural artifacts of the depth parameterization. This was not a primary consideration in GPR03, and so a somewhat rough model of V_{SH} and V_{SV} was obtained, with even more pronounced radial roughness when the model is converted to V_S and ξ (Fig. 6).

In the new model, a negative $\delta \ln \xi$ signature is apparent associated with the ridges between 200 and 300 km depth. For the fast-spreading ridges of the Pacific and Indian Oceans in particular, there appears to be a strong correlation between the amplitude of the negative $\delta \ln \xi$ signature and the spreading rate of the ridge. To quantify this relationship, we defined a series of ridge segments approximately 7.5° in length for all major mid-ocean ridges (Fig. 7). For each segment we compared the value of $\delta \ln \xi$ with the spreading rate. Spreading rates were calculated by taking the component of relative velocity perpendicular to each ridge segment as calculated using NUVEL-1

(DeMets *et al.* 1990) evaluated at the midpoint of each segment. For quantitative comparison purposes, we used all segments with spreading rates greater than 5 cm/yr (displayed in bold solid and dashed lines in Fig. 7), all of which are located in the Pacific and Indian Oceans. The spreading rates compared with $\delta \ln \xi$ values at 200 and 250 km depth are shown in Fig. 8. Most values are negative, although there are a few positive values for spreading rates less than 7.5 cm/yr. If we perform a linear regression on the correlation of the $\delta \ln \xi$ values at 200 and 250 km depth compared with the spreading rates, we fit the data with R^2 values (a measure of goodness-of-fit which ranges from 0 to 1, with 1 meaning a perfect fit) of 0.26 and 0.29, respectively. Given the number of segments used in the regression, both of these values represent a significant relationship between $\delta \ln \xi$ and spreading rate at or above the 99% confidence level according to an F-test. The p-values, which indicate the probability that the misfit of the linear regression is equivalent to a line with a slope of zero, are 0.006 and 0.003 for 200 and 250 km respectively. However, it appears that the segments nearest the subduction zones at the northern end of the East Pacific Rise, and the spreading segment between the Cocos and Nazca plates west of South America have anomalously low values of $\delta \ln \xi$, perhaps explained by interaction with the vertical flow of the nearby subduction zone. When these 4 segments (dashed lines in Fig. 7) are excluded from the regression analysis, the best-fit slopes become more strongly negative, and the R^2 values increase to 0.50 and 0.59 for 200 and 250 km depth, respectively. This represents a significant relationship above the 99.99% confidence level, with p-values less than 0.0001. This significant correlation between the variation of surface spreading rates along several ridge systems and amplitude of anisotropy at depth strongly supports development of $V_{SV} > V_{SH}$ due to vertical flow beneath fast-spreading mid-ocean ridges, although in some slower spreading regions, there remains the $V_{SH} > V_{SV}$ usually seen away from the ridges under oceanic regions due to horizontal deformation.

3.3 Transition zone anisotropy

While anisotropy at transition zone depth ranges (400-700 km) is not included in global models such as PREM (Dziewonski & Anderson 1981), several studies have indicated the possible presence of anisotropy in this depth range (Montagner & Kennett 1996; Fouch & Fischer 1996;

Trampert & van Heijst 2002; Beghein & Trampert 2003). While the amplitudes of anisotropy observed in our model are lower than those in the uppermost mantle (Fig. 9), there is a clear signature present in this depth range.

The most prominent feature of the model in this depth range (Fig. 10) is the association of negative ξ perturbation ($V_{SV} > V_{SH}$) with subduction zones. Below 400 km depth, there is a clear correlation of negative ξ perturbations both with the high isotropic velocities usually associated with slabs, as well as the predicted locations of slabs from a geodynamic model based on reconstructed subduction history over the last 180 million years (Lithgow-Bertelloni & Richards 1998) (Fig. 11). This signature fades rapidly below the 670 discontinuity, even though some isotropic velocity anomalies continue. These observations suggest that quasi-vertical flow in the subduction zones leads to observed anisotropy, perhaps through a mechanism related to alignment of spinel crystals or through alignment of pockets of strongly contrasting garnetetite derived from oceanic crust (Karato 1998b).

The ridge signal of negative ξ anomalies, which is prominent in the uppermost 300 km of the model, vanishes under most ridges, with the exception of the East Pacific Rise, where it appears to continue to approximately 500 km depth, although the isotropic anomaly does not extend to such depths. The lack of a similar $V_{SV} > V_{SH}$ signature under most mid-ocean ridges suggests that the vertical flow is confined to shallower depth than in subduction zones, as seen in isotropic velocity (Montagner & Ritsema 2001) and attenuation models (Romanowicz & Gung 2002).

Fouch and Fischer, [1996] also observed anisotropy in the transition zone depth range from shear wave splitting measurements of local S and teleseismic SKS associated with some (but not all) subduction zones in the Northwest Pacific. Specifically there was evidence for splitting extending to at least 480 km and perhaps through the transition zone into the uppermost lower mantle under the Southern Kuril arc (Sakhalin Island), as well as possibly beneath western Honshu in Japan. The anisotropy was constrained to shallower depths beneath the Izu-Bonin trench to the south, where our model also shows no negative ξ perturbation. As these were splitting measurements, they only measured azimuthal anisotropy in a horizontal plane, so the sense of anisotropy cannot be directly compared. The directions, however, ranged from roughly trench parallel to 35^o

from parallel, which is not consistent with the trench perpendicular azimuth which might be expected from a simple model of quasi-vertical flow coupled to the downgoing slab, as suggested by our radial anisotropic model. Likely the motion would have to be a combination of downward flow coupled to the slab and some trench parallel or sub-parallel shear, although the trench parallel component observed in splitting measurements, which have little depth resolution, may be primarily in the uppermost 200 km (Hall *et al.* 2000).

There are some differences when comparing our model to other global models of transition zone anisotropy. The degree 0 pattern of our model (Fig. 12) differs from Montagner & Kennett (1996) who inverted for 1D anisotropic structure and observed a signal of positive ξ perturbations above the 670 changing to negative perturbations below the 670. The depth range of the degree 0 signature relative to the 670 discontinuity, though, is possibly not well constrained in our model (see sections 3.4 and 4.3.2). While the earlier work on low-degree azimuthal anisotropy in the transition zone by Trampert and van Heijst (2002) is not directly comparable, we note that general amplitude levels of $\sim 2\%$ are compatible between these studies. Beghein and Trampert (2003) also look at radial anisotropy in the transition zone, although they do not present a single preferred structural model. They choose to look at the distribution of likely models grouped over large tectonically-defined regions, making a direct comparison difficult. While this approach does not obviously show the subduction-related anisotropic signature, their modelling only includes fundamental and overtone surface waves and the addition of body waves in our dataset greatly improves the sampling, particularly in subduction regions.

3.4 Mid-mantle anisotropy

The amplitude of anisotropic structure in the model in the bulk of the lower mantle is lower than that of both the lowermost mantle and the upper mantle. Mineral physics and seismology suggest that the bulk of the lower mantle is nearly isotropic (Meade *et al.* 1995). Meade *et al.* noted that the amount of shear-wave splitting observed above a subduction zone was nearly the same for direct waves, SKS waves, and ScS waves, ruling out large regions of azimuthal anisotropy in the bulk of the lower mantle below the downgoing slab. Although the radial anisotropy measured in this study

does not produce shear wave splitting, it is unlikely that large regions of radial anisotropy would exist in this depth range without accompanying azimuthal anisotropy. LPO mechanisms do not, in general, produce such a structure. Although purely horizontally aligned layers or inclusions with no tilt can produce radial anisotropy without significant azimuthal anisotropy, generating such a structure in the mid-mantle, where mass transfer is likely to be primarily vertical, is also doubtful.

Given this evidence that even relatively small anisotropy is unlikely in this region, we need to ask whether our modelling requires anisotropic structure in this depth range, and whether its inclusion has any effect on the structure in other depth ranges. To test this, we performed inversions starting from the isotropic portion of the velocity model used for inversion for source parameters, using the Harvard CMT sources and original data weighting to avoid bias towards our final post-source inversion model. We performed test inversions from this isotropic model where anisotropic structure was allowed at all depths, as well as tests with structure constrained to be isotropic in two depth ranges describing the mid-mantle, namely from 670 to 2400 km depth and between 1200 and 2400 km depth (Table 2 and Fig. 13). For the latter model (model D), there was negligible effect on the recovered structure in other depth ranges, and the change in fit to the data when comparing models was very small (Table 2). There was no change in the fit to the surface waveforms, and allowing anisotropy in this depth range only improved the data fit for the body waveforms by 0.26%. When the constraint of isotropy is extended up to 670 km depth, there is some tradeoff with structure in the lower portion of the upper mantle transition zone, with correlation to the fully anisotropic model dropping to 0.89 averaged over the transition zone. The primary difference in the anisotropic structure of the lower portion of the transition zone is in the degree 0 term, as the transition zone correlation is 0.97 compared to the fully anisotropic model when the degree 0 terms are neglected. The degree 0 positive $\delta \ln \xi$ immediately below the transition zone (Fig. 12) is shifted upward when the anisotropy is constrained to zero below 670 km. The change in fit to the data is slightly more pronounced when this constraint is applied, with the fully anisotropic model showing a 0.5% better fit to the overall data set, and a 0.9% better fit to the body waveforms.

3.5 Core-mantle boundary region anisotropy

The final model in the lowermost mantle (Fig. 14) is similar in low degrees to the model of anisotropic structure for the core-mantle boundary (CMB) region developed in Panning & Romanowicz (2004), hereafter referred to as PR04, which was constrained to degree 8 for lower-mantle ξ (Fig. 15). As in that model, the degree 0 term is prominent (Fig. 12), and corresponds to a positive ξ anomaly ($V_{SH} > V_{SV}$) on the order of 1% averaged throughout the depth range. The large-scale pattern is also similar (correlation coefficient of 0.74 averaged over the bottom 300 km), although there are notable differences beneath Antarctica and Africa, where the coverage is poorest (Fig. 2).

Although the model parameterization is the same in PR04, and the dataset is similar, the inversions leading to the two models differ primarily in two respects. The PR04 model was a single iteration model using Harvard CMT solutions, while multiple iterations were performed for the model discussed in this paper, as well as inversion for source parameters for most events. Even more importantly, the scaling of V_P and ρ to V_S and η and ϕ to ξ in the PR04 model was not correctly applied in the inversion code, with V_P and ρ scaling coefficients mistakenly interchanged with η and ϕ coefficients. Despite the considerable difference in scaling used, including a change of sign, the results are markedly similar. This suggests that the scaling used does not have a strong influence on the anisotropic structure in this depth region, except where the coverage is poorest, as might be expected given the low sensitivity of our dataset to ϕ and η structure, compared with ξ. To test this conclusion, we also performed inversions where no scaling is assumed and where the ϕ structure is derived from the anisotropic P model of Boschi & Dziewonski (2000) (with η scaled to ϕ) (section 4.3.2). All 3 models are quite similar in the CMB region (Fig. 16A-C), with differences primarily under Antarctica and Africa. Since the dataset has very little sensitivity to ϕ and η, it appears that the scaling assumptions only have a significant effect in regions of the model with the poorest coverage.

Previous studies have also shown that CMB topography can exhibit tradeoffs with anisotropic structure (Boschi & Dziewonski 2000). We started from the best-fitting degree 16 model and performed 2 inversion iterations for a degree 24 isotropic and degree 16 anisotropic model in-

cluding degree 16 structure on the CMB and 670 discontinuity (see section 4.3). The isotorpic and anisotropic velocity structure in the lowermost mantle showed very little difference from the model with no discontinuity topography (Fig. 16D). The degree 0 ξ term was not influenced by the inclusion of CMB topography, but there was some change in the relative amplitudes of the lateral anisotropic structure imaged in our model, with a slight decrease in the amplitude of the anomalous regions in the central and eastern Pacific, and a slight increase in the amplitude of the anomaly under central Asia.

In PR04, it was noted that the two broad regions that most deviated from the average degree 0 signature corresponded to the superplume regions of low isotropic velocity, although there were also regions of reduced ξ west of North America and under central Asia. In this improved model, although the pattern is very similar to PR04, it is apparent that the regions of negative and reduced ξ are clearly offset from the centers of the superplumes as defined by the isotropic velocity structure. Qualitatively, these regions appear to be more associated with the transitions from high to low velocities at the boundaries of the superplumes, particularly around the Pacific superplume, where the model is most consistent with previous work, and coverage is best. In the current model, the anisotropic signature of the African superplume is much less well-defined. As discussed above, the structure of this region appears to be sensitive to the assumed scaling relationships as well as CMB topography, and so conclusions about the anisotropic structure in this region are problematic. However, the preferred model does include a reduction in the positive $\delta \ln \xi$ signature under eastern Africa, corresponding to the region of highest gradient between fast and slow isotropic velocities.

Although these observations do not uniquely constrain the mineral physics or dynamics of the lowermost mantle, they remain suggestive of a model where considerable anisotropy is generated in the primarily horizontal flow at the mechanical boundary layer under downgoing slabs, either through a mechanism of LPO (McNamara *et al.* 2002; Iitaka *et al.* 2004; Tsuchiya *et al.* 2004) or SPO (Kendall & Silver 1996). In fact, recent theoretical and experimental studies have demonstrated the possible stability of post-perovskite phase of $MgSiO_3$ in the lowermost 300 km of the mantle (Iitaka *et al.* 2004; Tsuchiya *et al.* 2004). These studies show this phase to have a greater

single crystal elastic anisotropy at lowermost mantle pressures than the perovskite thought to make up the bulk of the lower mantle, at least for 0K theoretical work (Iitaka *et al.* 2004).

Regardless of the mechanism responsible for the horizontal flow signature under the slabs, as the material approaches regions of large-scale upwelling this signature changes, and we see a reduction in observed anisotropy, with some negative $\delta \ln \xi$ regions observed in the central and eastern Pacific. These signature changes do not align with the center of the superplume regions, but appear to be strongest near the edges as the structure transitions from high to low velocity. There are a number of possible mechanisms for this, including rotation of the anisotropic material (McNamara *et al.* 2002) or inclusions of vertically oriented melt pockets.

3.6 Source parameters

For the initial iterations of the inversion, the published Harvard CMT solutions were used. These solutions were derived using a longer period dataset and an isotropic shear velocity model. To improve the fit to the data, we invert for the 10 source parameters (latitude, longitude, and depth of the centroid, plus origin time and the 6 independent moment tensor elements), and use these revised solutions to further refine the structural model.

To avoid unrealistic solutions, we first constrained the explosive component of the moment tensor to 0 (as in the original Harvard CMT solutions used), reducing the number of unknowns by one. Because the source inversion is non-linear, we performed 3 iterations for each event. Of the 1191 events in our dataset, 1108 (93%) had sufficient data for a stable inversion which showed convergence. Before using these data for further structural inversions, we compared the resulting solutions to the original Harvard solutions. To compare the changes in mechanism, we use the moment tensor difference function (Pasyanos *et al.* 1996),

$$\mu = \sqrt{\frac{\sum_{i=1}^{3}\sum_{j=1}^{3}(M_{ij}^{(1)\prime} - M_{ij}^{(2)\prime})^2}{8}}$$

where $M'_{ij} = M_{ij}/M_0$ and M_0 is the scalar seismic moment. This function varies between 0 and 1, with 0 representing identical mechanisms, and 1 representing a double-couple with exactly the opposite sense of motion. For values of $\mu < 0.25$, the mechanisms are essentially the same,

while for $\mu > 0.5$, the mechanisms are significantly different. Only 4 of the inverted mechanisms had values of $\mu > 0.25$ and none had $\mu > 0.5$, indicating that the differences are small, as would be expected given the fact that the Harvard solutions were already good fits to the data.

However, there was a systematic bias in inverted M_0, with an average decrease in the final value of M_0 by 16% (or a decrease in M_W of 0.05) (Fig. 17). This bias is similar to the shift of 0.075 magnitude units when comparing regional estimates of M_W calculated by spectral and time-domain approaches (Pasyanos *et al.* 1996). It is also comparable to the 0.1 unit downward shift seen by Dziewonski & Woodhouse (1983) between the best fit relationship of M_W calculated from Harvard CMT solutions to M_S and the theoretical relationship between M_W and M_S (Kanamori 1977). In both cases above, the recovered moment is likely decreased in order to minimize misfit due to poor fits in phase relative to a method that does not require phase matching, such as spectral estimation of M_W or the determination of M_S. Because our dataset of body waveforms and surface waveforms with cutoff periods of 32 and 60 seconds respectively is higher frequency than that used by the Harvard CMT methodology (45 and 135 seconds), the bias due to difficulty in matching phase is even more pronounced.

Because the lower seismic moments recovered using the above method were likely biased, we performed the source inversion again, with the seismic moment fixed to that of the Harvard CMT solution, reducing the total number of unknowns per event to 8. Given this more constrained inversion, a smaller number of events converged with sufficient improvement in fit to the data (964 events or 80.9% of the events). Of these events only 2 had values of μ slightly greater than 0.25 (with values of 0.26 and 0.27), showing the changes in mechanism to once again be small when the scalar moment is fixed.

Location changes are also, in general, quite small. Depth shifts average less than 4 km, with no significant bias deeper or shallower. Horizontal location shifts average 0.015° with no single shift greater than 0.1°. When the vector shifts are summed in 5° by 5° cells, areas associated with active subduction zones around the Pacific show some constructive stacking (Fig. 18), suggesting systematic, albeit small, source relocation due to the improved structural model. When the shifts in Figure 18 are normalized by the number of events in each cell, the subduction zone shifts are

significantly reduced, as those cells have the highest event density, but the stacking in those cells is still significant. To demonstrate this significance, we can look at two quantities. The average azimuthal deviation, Θ, can be defined as

$$\Theta = \frac{1}{N}\sum_{i=1}^{N}|\theta_i - \theta_0|,$$

where N is the number of events in a cell, θ_i is the azimuth of the relocation of a single event, and θ_0 is the azimuth of the vector sum of all event relocations in the cell. We also define the stacking efficiency,

$$E = \frac{|\mathbf{V}|}{\sum_{i=1}^{N}|\mathbf{v}_i|},$$

where $|\mathbf{V}|$ is the magnitude of the vector sum of the cell's event relocations, and $|\mathbf{v}_i|$ is the magnitude of each event's relocation vector. For relocations that are all identical in direction $\Theta = 0^{\circ}$ and $E = 1.0$, while for a set of relocations that is sufficiently large and entirely random in magnitude and azimuth, we would expect $\Theta = 90^{\circ}$ and $E = 0.0$. For the 14 cells with a vector-summed location shift with a magnitude greater than 0.1°, the average value of Θ, weighted by number of events in the cell, was 4.6°, and the average value of E was 0.58. In order to demonstrate that this degree of stacking is systematic, we performed the vector sum on 100,000 realizations of the event relocations in these 14 cells given the same magnitude of offsets, but random azimuths (i.e. no systematic offsets). The mean value of Θ was 90.2°. 99.9% of the random realizations had $\Theta > 71.4^{\circ}$. The mean value of E was 0.31, and 99.9% had $E < 0.44$. We can say with a high level of confidence that the source inversions with the improved velocity model are systematic.

4 MODEL RESOLUTION AND ERROR

4.1 Resolution matrix tests

A common way of analyzing the resolution of a model from a least-squares inversion is to utilize the resolution matrix. Using this approach, it is possible to get an idea of the model resolution given the dataset's sensitivity, and the *a priori* damping scheme applied. It does not, however, assess uncertainties resulting from the theoretical approximations in the partial derivative calculation, or

due to errors in the data aside from the effect of the *a priori* data covariance matrix applied as a weighting factor to the data points in the inversion.

Given these limitations, this approach allows us to perform the standard 'checkerboard' tests to obtain an estimate of the geographical resolution of the model parameters. The isotropic velocity model is well-resolved through degree 16 in the whole mantle and through degree 24 in the upper mantle. Figure 19 shows the output model for an input degree 24 pattern in the upper mantle and degree 16 in the lower mantle (Fig. 19A) at a variety of depths both with (Fig. 19C) and without (Fig. 19B) anisotropy in the input model. The pattern is well captured, although there is some reduction in amplitude. The resolution for ξ is, not surprisingly, not as good (Fig. 20). The highest degree structure is not resolved at all, except in the shallowest depth ranges. For the lowermost mantle, the input checkerboard model shown in Fig. 20A only includes degree 4 structure. The pattern of structures up to approximately degree 10 is also recovered (not shown), but the amplitudes are reduced strongly. In some depth ranges, there also appears to be some amount of tradeoff with unmodelled isotropic velocity structure, as shown in Figure 20C, in which the input model also contains isotropic structure equivalent to the input model shown in Figure 19A. This effect is most noticeable in the lower transition zone and uppermost lower mantle, as well as to a lesser extent in the southern hemisphere in the lowermost mantle.

We also tested the depth resolution of the modelling. We used an input model of random ξ structure with a white spectrum through degree 16, and compared the input and output amplitude as a function of depth (Fig. 21). For each depth range, there is some amount of smearing. Notably, a small percentage of mid-mantle structure is mapped into the transition zone (Fig. 21D-F). This is probably not a large concern, as anisotropic structure in the mid-mantle is expected to be negligible, but it is important to be aware of it when interpreting transition zone structure. Structure in either of the two splines corresponding to the deepest mantle (Fig. 21G,H) maps into a similar pattern with a peak at the CMB. This confirms the poor resolution of the depth distribution of anisotropy in the lowermost mantle discussed in PR04.

4.2 Bootstrap and jackknife error estimates

Formal errors are difficult to calculate for model parameters in a damped least-squares inversion. One way to estimate the model errors, given our inversion process is through a bootstrap approach (Efron & Tibishirani 1993). The bootstrap is a general statistical approach to calculating the standard error of the value of any estimator, θ. In our case, θ is the set of partial derivative and matrix calculations leading from the dataset of seismic waveforms to our model. The bootstrap standard error is calculated by applying the estimator to a sufficiently large set of random samples of the data, and analyzing the standard deviation of the models estimated from each sample. Although, our dataset has millions of points (Table 1), we simplify this approach by considering 12 subsets of the data formed by separating the data by the month of the event, and considering those as our sample population. A bootstrap sample is then any set of 12 subsets selected from that population with replacement. For any set of n observations, there are n^n bootstrap samples, although many of these are exchangeable (i.e. $x_1, x_2, ...x_n$ is the same as $x_2, x_1, ...x_n$). Even taking into account that exchangeability, there are more than 1,300,000 possible bootstrap samples of our 12 subsets, which is far too many to reasonably calculate, but the bootstrap approach will in general converge relatively quickly. We choose to make 300 bootstrap resamples, and then generate maps of the estimated errors (Fig. 22).

A similar approach which is somewhat less computationally intensive is the delete-d jackknife error estimation. In this approach, the model is calculated for a series of n datasets which leave out d observations at a time, and the standard error is calculated as

$$\hat{se}_{jack} = \sqrt{\frac{n-d}{d \cdot C(n,d)} \sum (\theta_{(i)} - \bar{\theta})},$$

where $C(n,d)$ is combinatorial notation indicating the number of subsets of size d from a population of n chosen without replacement, the sum is over the $C(n,d)$ possible jackknife samples of the dataset, $\theta_{(i)}$ is the estimator value for the ith jackknife sample, and $\bar{\theta} = \sum \theta_{(i)}/(C(n,d))$. This is basically the standard deviation of the models multiplied by an inflation factor roughly equal to n for $d = 1$ and smaller values for $d > 1$, where the datasets are less similar to the original dataset.

If we use the same 12 subsets as above, only 12 models need to be calculated for $d = 1$, or 66 for $d = 2$.

All three estimates of the error in the maps are virtually identical, with a correlation above 0.99 at all depth ranges, and amplitudes within a few percent. Therefore we only show the error maps from the bootstrap approach. The consistency of the three estimates is a cross-check that we performed enough bootstrap resamples. The error estimate for isotropic V_S is consistently low throughout the mantle, with a small increase in the lowermost mantle (compare error amplitude in Fig. 22K with model amplitude in Fig. 9). In pattern, the error in this lowermost depth ranges appears to mirror the coverage in Figure 2, with slightly larger error estimates in the southern hemisphere particularly under Africa and the eastern Pacific. The ξ errors are larger in the upper mantle, but similar to the errors in V_S in the lower mantle, with a slight increase in the lowermost mantle. The pattern is different, though, with the largest error in the upper mantle being roughly correlated with strong gradients in structure. In the lower mantle, the regions of greatest error are correlated with the regions with the strongest ξ signal, suggesting the uncertainty is chiefly in amplitude, rather than lateral pattern.

This approach to error estimation, like the resolution matrix testing, also does not directly treat errors related to the changes in the choice of damping or theoretical assumptions. These error maps show how random errors in the data will map into the observed structure, given the damping and inversion scheme used to develop the model.

4.3 Other possible sources of error

4.3.1 Crustal correction and other discontinuities

An important consideration in any study of mantle structure is that of corrections for crustal structure. In our modelling, we use a somewhat ad-hoc method to describe the anisotropic crustal structure. For the transverse component data we correct the data for the topography of the seafloor and Moho discontinuities derived from the modelling of transverse component data in the development of SAW24B16 (Mégnin & Romanowicz 2000). For the vertical and radial component data,

we use the discontinuity perturbations of *CRUST 5.1* (Mooney *et al.* 1998), which were derived using Rayleigh waves, and are thus more appropriate for V_{SV} sensitive data.

To test what kind of effects this simplified approach has on our recovered velocity models, we replaced the separate crustal models with a single one defined by the average of the two, and inverted simultaneously for velocity and perturbations to the seafloor and Moho discontinuities, using the Harvard source mechanisms. Changing the crustal model led to a 9.8% decrease in variance reduction, which was primarily due to the 21% decrease in variance reduction for the fundamental mode surface waves, while the overtone surface waves saw little change in fit, and the body waves saw a 4.7% decrease in variance reduction. The resulting mantle velocity model, however, was similar. The isotropic velocity model was correlated at an average of 0.89 for the whole mantle, with a minimum of 0.77 occurring in the transition zone at ~500 km (Fig. 23A). The changes in ξ were slightly larger, with an average correlation of 0.80 across the depth range, with more significant decreases in correlation around 1600, 2100 and 2600 km depth dropping as low as 0.4 in the vicinity of 1600 and 2600 km depth. These depths, however, correspond to changes from positive to negative degree 0 ξ anomalies, which are slightly offset with the more simplified crustal model. When the degree 0 terms are neglected, the correlation is above 0.8 throughout the mantle, with the exception of a small decrease between 1200 and 1800 km depth.

The 670 discontinuity and the core-mantle boundary also likely have significant topography. To test the possible tradeoffs with isotropic and anisotropic velocity structure, we did a two iteration model inversion for discontinuity topography of the 670 and CMB parameterized to degree 16, starting from the best-fitting degree 16 model and the dataset including revised source parameters. This is the same starting model and dataset used in developing the final degree 24 isotropic and degree 16 anisotropic model. The volumetric velocity model has the same parameterization as the final model.

The particular dataset is not chosen to maximize sensitivity to the CMB topography. The CMB sensitive dataset is dominated by reflected and diffracted phases with less contribution from transmitted phases. Given these limitations, we set the damping so as to match the VLBI constraint on the excess ellipticity of the CMB (Gwinn *et al.* 1986; Forte *et al.* 1995), determined from

modelling the Earth's nutations. This can be expressed by the degree 2 zonal coefficient, which for spherical harmonics, normalized according to Edmonds (1960), is equal to a value of -0.52 $\pm$ 0.12 km. The overall amplitudes obtained of $\sim \pm$ 1.6 km (Fig. 24A), however, are lower than previous seismic studies of CMB topography (Morelli & Dziewonski 1987; Boschi & Dziewonski 2000), which show amplitudes of $\sim \pm$ 5-10 km. On the very large scale, there is some agreement in pattern with depressions under the western Pacific and South American subduction zones, and elevation under the central Pacific and Africa. The large uplift under western North America, and depression under central Eurasia do not agree as well with previous seismic models, and their amplitudes may be artifacts of the dataset sensitivity, although there is some sign of these features in geodynamic modelling of CMB topography (Forte *et al.* 1995).

We also do not explicitly select packets with SS precursors that would give us sensitivity to the 670 topography. These phases are present, however, within many SS packets, and there is also sensitivity in some regions due to the presence of wavepackets from deep events with the multiple ScS reverberative interval (Appendix B). We therefore apply fairly strong horizontal smoothing to obtain wavelengths of features comparable to previous studies (Flanagan & Shearer 1998; Gu *et al.* 2001). Due to this damping, the recovered amplitudes of $\sim \pm$ 10 km (Fig. 24B) are somewhat smaller than the $\sim \pm$ 15-20 km recovered from SS precursor studies. The patterns are broadly consistent with the previous work, with a more shallow mean depth than the 670 km in PREM, and depression below western Pacific subduction zones, and elevation beneath the Pacific and parts of Africa, although the elevated region west of the western Pacific subduction zones does not appear in those models, and there are significant differences under South America and Australia.

While the dataset sensitivity may not currently be sufficient to fully resolve global topography on these discontinuities, there does not appear to be significant tradeoffs with the isotropic and anisotropic velocity structure (Fig. 23B). There are some minor changes in the isotropic velocity near the 670, and there are some small amplitude changes in the anisotropic pattern near the CMB (Fig. 16D), but these appear to be negligible. Specifically selecting wavepackets with sensitivity to these structures, as well as including higher frequency data may increase our ability to resolve this structure using our methodology in the future, but of course the potential tradeoffs with velocity

structure could likewise increase. The fact that we are able to detect some of the discontinuity signal bodes well for the future of our finite frequency waveform approach.

4.3.2 Scaling parameters

The anisotropic scaling parameters used in our modelling were derived for deformation of upper mantle materials above 400 km (Montagner & Anderson 1989). Obviously, it is reasonable to question the validity of this scaling assumption at greater depths. To test the influence of the assumed scaling parameters on our model, we performed tests with the ϕ model fixed to that of Boschi and Dziewonski (2000). We then scaled the 3D η structure to this ϕ model. For our first test, we fixed the ϕ and η structures, and then inverted the pre-source inversion dataset for ξ structure starting from a model with no ξ perturbations. We also performed an inversion where the ξ, ϕ, and η structures were simultaneously inverted starting from the ξ model used in the source inversions, and the ϕ and η model described above. We also attempted an inversion for all 3 anisotropic parameters starting from an initially isotropic model, but the very small ϕ and η sensitivities of our dataset led to a very unstable inversion, which we do not consider further here.

In general, the correlation of the ξ models derived in these tests agreed well with the final, preferred ξ model (Fig. 25), especially in the lowermost mantle. The strongest deviations occur for the fixed ϕ and η model in the region immediately above and below the 670 discontinuity. The structures of this model look quite different at a depth of 670 km than that of the preferred model, and the positive degree 0 signature shifts from below to above the 670 discontinuity. This suggests that this region could exhibit strong tradeoffs with ϕ and η structure, as well as potentially unmodeled azimuthal anisotropy. It is also possible that this instability could be related to a distinct change in structure characteristics on either side of the 670 discontinuity (e.g. (Gu *et al.* 2001)) which is unmodelled in our smooth radial spline parameterization. In any case, interpretation of anisotropy in the lower transition zone and uppermost lower mantle should be undertaken with a degree of caution.

4.3.3 Model Parameterization

For our final model, we chose to parameterize shear velocity anisotropy in terms of the Voight average isotropic velocity and ξ. Some previous models of anisotropy, particularly in the upper mantle have preferred a parameterization with separate V_{SV} and V_{SH} models (Ekström & Dziewonski 1998; Gung *et al.* 2003). This is a natural parameterization choice for models with a large fundamental mode surface wave dataset, as the parameterization directly mirrors the sensitivity of the dataset. However, with a dataset also containing overtone surface waves and body waves to model whole mantle structure, the division of dataset sensitivity is no longer so obvious, and damping considerations favor a model where we invert directly for the anisotropy, so as to not map errors in amplitude of velocity structure into an anisotropic signature. We also performed a test inversion where we inverted for V_{SV} and V_{SH} separately, starting from V_{SV} and V_{SH} models converted from our final V_S and ξ models. The damping for this inversion started from the damping used for the isotropic velocity, and was tuned to produce radially smooth V_{SV} and V_{SH} models similar in amplitude as a function of depth. This model was converted back to V_S and ξ for comparison with our preferred model.

The isotropic average of the V_{SV}/V_{SH} model was very consistent with our preferred isotropic model, with an average correlation coefficient of 0.96 as a function of depth, and no depth range having a correlation coefficient of less than 0.91 (Fig. 26A).

In the uppermost mantle, the anisotropic portion also showed similar stability with an average correlation coefficient of 0.96 above 400 km. The correlation over the transition zone was a little lower, averaging 0.86 between 400 and 700 km. This difference appears to be mostly in the lower transition zone, and is also partially explained by a shift in the degree 0 term (correlation improves to 0.89 when degree 0 terms are neglected), which appears to be sensitive to tradeoffs.

The lower mantle anisotropic structure is less well-correlated, particularly in the depth range from 1200 to 2000 km. There is also a pronounced increase in the amplitude and radial roughness of recovered anisotropy in the lower mantle, when we are not directly damping ξ (Fig. 26B). This large amplitude signature in the mid-mantle depth ranges is hard to reconcile with studies showing negligible anisotropy in the bulk of the lower mantle. The lowermost mantle anisotropy derived

from the V_{SV}/V_{SH} model has a similar degree 0 profile as the preferred model, but has higher amplitudes of 3D heterogeneity, meaning the regions of $V_{SV} > V_{SH}$ under the central and eastern Pacific are more pronounced. There is also a strong $V_{SV} > V_{SH}$ under southern and northwestern Africa.

5 CONCLUSIONS

While the isotropic velocities of SAW24AN16 are compatible with previous tomographic models of shear velocity structure and are quite stable regardless of the anisotropic structure, the anisotropic portion of the model can be related to mantle flow patterns in several depth ranges throughout the mantle.

Specifically, a positive $\delta \ln \xi$ signature appears consistent with a region of likely horizontal flow under the lithosphere at different depths for oceans and old continents (Gung *et al.* 2003). A negative $\delta \ln \xi$ signature at 200-300 km depth is associated with spreading ridge segments, and the amplitude is significantly correlated with surface spreading rates for fast-spreading segments. There is also negative $\delta \ln \xi$ correlated with subducting slabs in the transition zone, although this depth range appears to be sensitive to tradeoffs with unmodelled anisotropic velocity parameters. Mid-mantle anisotropy is lower in amplitude, and its inclusion does not significantly affect the patterns obtained in other depth ranges. The structure near the CMB is dominated by a degree 0 positive $\delta \ln \xi$, likely due to horizontal flow in a mechanical boundary layer, with deviations associated with transition to the low-velocity superplumes.

Although the current dataset cannot provide us with anisotropic resolution at the same level as global isotropic velocity models, and some tradeoffs with parameters not modelled here remain, the additional information can help constrain geodynamic models, as well as providing an opportunity to verify and guide the experimental and theoretical findings of mineral physics.

ACKNOWLEDGMENTS

The authors would like to acknowledge Thorsten Becker and Caroline Beghein for helpful comments and suggestions. Lapo Boshi and Carolina Lithgow-Bertelloni also provided models for use

in this paper. This research was supported by NSF grant EAR-0308750. All figures were made with GMT (Wessel & Smith 1998). This is contribution 04-XX of the Berkeley Seismological Laboratory.

REFERENCES

Babuska, V. & Cara, M., 1991. *Seismic Anisotropy in the Earth*, Kluwer Academic Press, Boston.

Beghein, C. & Trampert, J., 2003. Probability density functions for radial anisotropy: implications for the upper 1200 km of the mantle, *Earth Planet. Sci. Lett.*, **217**, 151-162.

Beghein, C. & Trampert, J., 2004. Probability density functions for radial anisotropy from fundamental mode surface wave data and the Neighbourhood Algorithm, *Geophys. J. Int.*, **157**, 1163-1174.

Boschi, L. & Dziewonski, A., 2000. Whole Earth tomography from delay times of P, PcP, PKP phases: lateral heterogeneities in the outer core, or radial anisotropy in the mantle?, *J. Geophys. Res.*, **104**, 25267-25594.

Daradich, A., Mitrovica, J.X., Pysklywec, R.N. Willett, S.D. & Forte, A.M., 2003. Mantle flow, dynamic topography, and rift-flank uplift of Arabia , *Geology*, **30**, 901-904.

DeMets, C., Gordon, R.G., Argus, D.F., & Stein, S., 1990. Current plate motions, *Geophys. J. Int.*, **101**, 425-478.

Dziewonski, A.M. & Anderson, D.L., 1981. Preliminary Reference Earth Model, *Phys. Earth Planet. Inter.*, **25**, 297-356.

Dziewonski, A.M. & Woodhouse, J.H., 1983. Studies of the seismic source using normal-mode theory, in *Earthquakes: observation, theory and interpretation*, pp. 45-137, eds. Kanamori, H. & Boschi, E., North-Holland Publ. Co., Amsterdam.

Edmonds, A.R., 1960. *Angular momentum in quantum mechanics*, Princeton University Press, Princeton, New Jersey.

Efron, B. & Tibishirani, R.J., 1991. *An Introduction to Bootstrap*, Chapman and Hall, New York.

Ekström, G. & Dziewonski, A.M., 1998. The unique anisotropy of the Pacific upper mantle, *Nature*, **394**, 168-172.

Flanagan, M.P. & Shearer, P.M., 1998. Global mapping of topography on transition zone velocity discontinuities by stacking SS precursors, *J. Geophys. Res.*, **103**, 2673-2692.

Forte, A.M., Mitrovica, J.X., & Woodward, R.L., 1995. Seismic-geodynamic determination of the origin of excess ellipticity of the core-mantle boundary, *Geophys. Res. Lett.*, **22**, 1013-1016.

Fouch, M.J. & Fischer, K.M., 1996. Mantle anisotropy beneath northwest Pacific subduction zones, *J. Geophys. Res.*, **101**, 15987-16002.

Garnero, E.J. & Lay, T., 1997. Lateral variations in lowermost mantle shear wave anisotropy beneath the north Pacific and Alaska, *J. geophys. Res.,* , **102**, 8121-8135.

Grand, S., 1997. Global seismic tomography: a snapshot of convection in the Earth, *GSA Today*, **7**, 1-7.

Gu, Y.J., Dziewonski, A.M., Su, W., & Ekström, G., 2001. Models of the mantle shear velocity and discontinuities in the pattern of lateral heterogeneities, *J. Geophys. Res.*, **106**, 11169-11199.

Gung, Y., 2003. *Lateral variations in attenuation and anisotropy of the upper mantle from seismic waveform tomography*, Ph.D. thesis, University of California at Berkeley, Berkeley, CA.

Gung, Y., Panning, M., & Romanowicz, B., 2003. Global anisotropy and the thickness of continents, *Nature*, **422**, 707-711.

Gwinn, C.R., Herring, T.A., & Shapiro, I.I., 1986. Geodesy by radio interferometry: Studies of the forced nutations of the Earth, 2. Interpretation, *J. Geophys. Res.*, **91**, 4755-4765.

Hall, C.E., Fischer, K.M., Parmentier, E.M., & Blackman, D.K., 2000. The influence of plate motions on three-dimensional back arc mantle flow and shear wave splitting, *J. Geophys. Res.*, **105**, 28009-28033.

Hess, H., 1964. Seismic anisotropy of the uppermost mantle under oceans, *Nature*, **203**, 629-631.

Hager, B.H., 1984. Subducted slabs and the geoid - constraints on mantle rheology and flow, *J. geophys. Res.,* , **89**, 6003-6015.

Iitaka, T., Hirose, K., Kawamura, K, & Murakami, M., 2004. The elasticity of the $MgSiO_3$ post-perovskite phase in the Earth's lowermost mantle, *Nature*, **430**, 442-445.

Kanamori, H., 1977. The energy release in great earthquakes, *J. Geophys. Res.*, **82**, 2981-2987.

Karato, S.-I., 1998a. Some remarks on the origin of seismic anisotropy in the D" layer, *Earth Planets Space*, **50**, 1019-1028.

Karato, S.-I., 1998b. Seismic anisotropy in the deep mantle, boundary layers and the geometry of mantle convection, *Pure Appl. Geophys.*, **151**, 565-587.

Kawasaki, I. & Konno, F., 1984. Azimuthal anisotropy of surface waves and the possible type of seismic anisotropy due to preferred orientation of olivine in the uppermost mantle beneath the Pacific ocean, *J. Phys. Earth*, **32**, 229-244.

Kendall, J.-M. & Silver, P. G., 1996. Constraints from seismic anisotropy on the nature of the lowermost mantle, *Nature*, **381**, 409-412.

Lay, T. & Helmberger, D.V., 1983. The shear-wave velocity gradient at the base of the mantle, *J. geophys. Res.,* , **88**, 8160-8170.

Lay, T., Williams, Q., Garnero, E.J., Kellogg, L., & Wysession, M.E., 1998. Seismic wave anisotropy in the D" region and its implications, in *The Core-Mantle Boundary Region*, pp. 299-318, eds. Gurnis, M., Wysession, M.E., Knittle, E., & Buffett, B.A., Amer. Geophys. Union, Washington, D.C.

Li, X.D. & Romanowicz, B., 1995. Comparison of global waveform inversions with and without considering cross-branch modal coupling, *Geophys. J. Int.*, **121**, 695-709.

Li, X.D. & Romanowicz, B., 1996. Global mantle shear velocity model developed using nonlinear asymptotic coupling theory, *J. Geophys. Res.*, **101**, 22245-22272.

Li, X.D. & Tanimoto, T., 1993. Waveforms of long-period body waves in a slightly aspherical Earth model, *Geophys. J. Int.*, **112**, 92-102.

Lithgow-Bertelloni, C. & Richards, M.A., 1998. The dynamics of Cenozoic and Mesozoic plate motions, *Rev. Geophys.*, **36**, 27-78.

Love, A.E.H., 1927. *A Treatise on the Theory of Elasticity*, Cambridge Univ. Press, Cambridge.

Masters, G., Laske, G., Bolton, H., & Dziewonski, A., 2000. The relative behavior of shear velocity, bulk sound speed, and compressional velocity in the mantle: implications for chemical and thermal structure, in *Earth's Deep Interior*, AGU Monograph 117, pp. 63-86, eds. Karato, S., Forte, A.M., Liebermann, R.C., Masters, G., & Stixrude, L., Amer. Geophys. Union, Washington, D.C.

Matzel, E., Sen, K., & Grand, S.P., 1997. Evidence for anisotropy in the deep mantle beneatch Alaska, *Geophys. Res. Lett.,* , **23**, 2417-2420.

McEvilly, T.V., 1964. Central U.S. crust-upper mantle structure from Love and Rayleigh wave phase velocity inversion, *Bull. Seism. Soc. Amer.*, **54**, 1997-2015.

McNamara, A.K., van Keken, P.E., & Karato, S.-I., 2002. Development of anisotropic structure in the Earth's lower mantle by solid-state convection, *Nature*, **416**, 310-314.

Meade, C., Silver, P.G., & Kaneshima, S., 1995. Laboratory and seismological observations of lower mantle isotropy, *Geophys. Res. Lett.*, **22**, 1293-1296.

Mégnin, C. & Romanowicz, B.A., 2000. The 3D shear velocity structure of the mantle from the inversion of body, surface and higher mode waveforms, *Geophys. J. Int.*, **143**, 709-728.

Menke, W. H., 1989. *Geophysical Data Analysis: Discrete Inverse Theory, Revised Ed.,* Academic Press, Inc., New York.

Mochizuki, E., 1986. The free oscillations of an anisotropic and heterogeneous Earth, *Geophys. J. R. astr. Soc.,* , **86,** 167-176.

Montagner, J.-P. & Anderson, D.L., 1989. Petrological constraints on seismic anisotropy, *Phys. Earth Planet. Inter.*, **54**, 82-105.

Montagner, J.-P. & Kennett, B.L.N., 1996. How to reconcile body-wave and normal-mode reference earth models, *Geophys. J. Int.*, **125**, 229-248.

Montagner, J.-P. & Ritsema, J., 2001. Interactions between ridges and plumes, *Science*, **294**, 1472-1473.

Montagner, J.-P. & Tanimoto, T., 1991. Global upper mantle tomography of seismic velocities and anisotropies, *J. Geophys. Res.*, **96**, 20337-20351.

Mooney W.D., Laske, G., & Masters, G., 1998. Crust 5.1: a global crustal model at $5\deg \times 5\deg$, *J. geophys. Res.,* , **103,** 727-747.

Morelli, A. & Dziewonski, A.M., 1987. Topography of the core-mantle boundary and lateral homogeneity

of the liquid core, *Nature*, **325,** 678-683.

Nataf, H.-C., Nakanishi, I., & Anderson, D.L., 1986. Measurements of mantle wave velocities and inversion for lateral heterogeneities and anisotropy: 3. inversion, *J. Geophys. Res.*, **91**, 7261-7307.

Panning, M.P. & Romanowicz, B.A., 2004. Inferences on flow at the base of Earth's mantle based on seismic anisotropy, *Science*, **303**, 351-353.

Pasyanos, M.E., Dreger, D.S. and Romanowicz, B., 1996. Toward real-time estimation of regional moment tensors, *Bull. Seism. Soc. Am.*, **86**, 1255-1269.

Pulliam, J and Sen, M.K., 1998. Seismic anisotropy in the core-mantle transition zone, *Geophys. J. Int.,* , **135**, 113-128.

Revenaugh, J. & Jordan, T.H., 1987. Observations of first-order mantle reverberations, *Bull. seism. Soc. Am.,* , **77**, 1704-1717.

Ricard, Y. & Vigny, C., 1989. Mantle dynamics with induced plate tectonics, *J. Geophys. Res.*, **94**, 17543-17560.

Ritsema, J. & van Heijst, H.-J., 2000. Seismic imaging of structural heterogeneity in Earth's mantle: evidence for large-scale mantle flow, *Science Progress*, **83**, 243-259.

Romanowicz, B. & Gung, Y., 2002. Superplumes from the core-mantle boundary to the lithosphere; implications for heat flux, *Science*, **296**, 513-516.

Romanowicz, B. & Snieder, R., 1988. A new formalism for the effect of lateral heterogeneity on normal modes and surface waves-II. General anisotropic perturbation, *Geophys. J. Int.,* , **93**, 91-99.

Russell, S.A., Lay, T., & Garnero, E.J., 1999. Small-scale lateral shear velocity and anisotropy heterogeneity near the core-mantle boundary beneath the central Pacific imaged using broadband ScS waves, *J. geophys. Res.,* , **104,** 13,183-13,199.

Silver, P.G., 1996. Seismic anisotropy beneath the continents: probing the depths of geology, *Annu. Rev. Earth Planet. Sci.*, **24**, 385-432.

Tanimoto, T. & Anderson, D.L., 1985. Lateral heterogeneity and azimuthal anisotropy of the upper mantle: Love and Rayleigh waves 100-250 s, *J. geophys. Res.,* , **90**, 1842-1858.

Tarantola, A. & Valette, B., 1982. Generalized nonlinear inverse problems solved using the least squares criterion, *Rev. Geophys. Space Phys.*, **20**, 219-232.

Trampert, J. & van Heijst, H.J., 2002. Global azimuthal anisotropy in the transition zone, *Science*, **296,** 1297-1299.

Tsuchiya, T., Tsuchiya, J., Umemoto, K., & Wentzcovitch, R.M., 2004. Elasticity of post-perovskite $MgSiO_3$, *Geophys. Res. Lett.,* , **31**, L14603, doi:10.1029/2004GL020278.

Vinnik, L.P., Farra, V., & Romanowicz, B.A., 1989. Observational evidence for diffracted SV in the shadow of the Earth's core, *Geophys. Res. Lett.,* , **16,** 519-522.

Vinnik, L.P., Makeyeva, L.I., Milev, A., & Usenko, Y., 1992. Global patterns of azimuthal anisotropy and

deformations in the continental mantle, *Geophys. J. Int.*, **111**, 433-447.

Wessel, P. & Smith, W.H.F., 1998. New, improved version of Generic Mapping Tools released, *EOS Trans. Amer. Geophys. Union*, **79**, 579.

Woodhouse, J.H., The coupling and attenuation of nearly resonant multiplets in the earth's free oscillation spectrum, *Geophys. J. R. astr. Soc.,* , **61**, 261-283.

Woodward, R.L., Forte, A.M., Su, W.J., & Dziewonski, A.M., 1993. Constraints on the large-scale structure of the Earth's mantle, in *Evolution of the Earth and Planets*, pp. 89-109, eds. Takahashi, E., Jeanloz, R., & Rubie, D., Amer. Geophys. Union, Washington, D.C.

Table 1. Summary of wavepackets used in inversion

Wavepacket type	Component	Min. period (s)	wavepackets	data points
Body	Z	32	12,469	274,927
Body	L	32	9,672	207,283
Body	T	32	15,076	160,627
Surface	Z	60	36,100	2,101,379
Surface	L	60	16,373	984,183
Surface	T	60	21,101	802,913
Surface	T	80	9,824	111,719
	Total		120,615	4,643,031

For component column, Z refers to vertical, L to longitudinal (along the great circle path between source and receiver), and T to transverse (perpendicular to L). The maximum period for each wavepacket is determined by event magnitude and ranges from 220s to 1 hour. The 80s T surface waves represent the surface wave dataset of Li and Romanowicz (1996).

Table 2. Correlation of ξ for constrained models to fully anisotropic model and change in fit to data

	Model				
Depth range	A	B	C	D	E
25-200	0.985	0.997	0.999	0.999	-
200-700	-	0.932	0.934	0.999	-
700-1200	-	-	-	0.999	-
1200-2400	-	-	-	-	-
2400 - 2891	-	-	0.970	0.989	-
Data	Change in data fit (%)				
Body	-2.52	-1.41	-1.11	-0.26	-8.69
Surface	-0.58	-0.34	-0.33	0.0	-9.42
Total	-1.35	-0.77	-0.64	-0.10	-9.13

Model letters are the same as in Fig. 13 with constrained depth regions marked as ”-”. Model E is the isotropic starting model for all the test models. Although the correlation curves in Fig. 13 show non-zero values at borders of constrained regions as an artifact of the spline parameterization, those values are not reported here. Changes in fit are the ratio of estimated data variance for each model for the body wave, surface wave, and full dataset relative to the data variance estimated for the fully anisotropic inversion.

Figure 1. Kernels describing sensitivity to V_{SH} (top), V_{SV} (2nd row), isotropic V_S (3rd row), and ξ (bottom row) for the phases S_{diff} (left) and ScS2 (right), all recorded on the transverse component. White represents positive values, black is negative, and grey is zero. The ξ kernels are multiplied by 4 to display on the same scale. The source is represented by a star, and the receiver by a triangle. The ray path from ray theory is shown as a black line. Note the dominance of V_{SH} sensitivity in the horizontally propagating S_{diff}, and V_{SV} in the vertical ScS2. Likewise, ξ sensitivity is the same sign as V_S for S_{diff}, but the opposite sign for ScS2.

Figure 2. Coverage calculated from the summed NACT kernels of the inversion dataset, as discussed in section 2.2. The isotropic V_S and ξ coverage is shown for 200 km thick layers in the upper mantle (A,D), lower transition zone (B,E), and lowermost mantle (C,F). The total sensitivity in each 200 km layer is shown as function of depth (G).

Figure 3. Isotropic V_S model at several depths.

Figure 4. Correlation of isotropic velocity model with previously published V_S tomographic models.

Figure 5. Comparison between SAW24AN16 ξ from this paper (A-C) and the upper mantle ξ calculated from SAW16AN (Gung *et al.* 2003) (D-F) at depths of 100 (top), 200 (middle), and 300 km (bottom).

Figure 6. Uppermost mantle RMS amplitude profiles for SAW16AN calculated for V_{SV} and V_{SH} (A) and V_S and ξ (B), and for SAW24AN16 V_S and ξ (C). Note the greater radial roughness of the SAW16AN profiles, particularly in ξ.

Figure 7. Fast-spreading ridge segments used in spreading rate calculations. Segments in bold solid and dashed lines represent all segments with spreading rates faster than 5 cm/yr used in Fig. 8. The dashed segments on the northern EPR and the Cocos/Nazca boundary are also shown in Fig. 8, but are excluded in some regression calculations.

Figure 8. Spreading rate vs. model $\delta \ln \xi$ value for the segments shown in Fig. 7. Segments used for linear regression are shown with diamonds, while the 4 segments nearest subduction zones not used in the regression (dashed segments in Fig. 7) are triangles. Model $\delta \ln \xi$ values are shown at 200 km (open symbols) and 250 km (filled symbols), and the regression lines are shown for the data at 200 km (solid) and 250 km (dashed).

Figure 9. RMS amplitudes as a function of depth in SAW24AN16 for V_S (solid) and ξ (dashed).

Figure 10. $\delta \ln \xi$ slices at 400, 500, 600, and 700 km depths.

Figure 11. ξ (top), V_S (middle) structure at depths of 400 (left) and 600 km (right). The bottom row shows the density anomalies for 145 km thick layers centered at depths of 362.5 km (left) and 652.5 km (right) for the model of Lithgow-Bertelloni and Richards (1998), normalized to the maximum density anomaly in each depth range.

Figure 12. Degree 0 (radially symmetric) ξ structure as a function of depth.

Figure 13. Model correlation to fully anisotropic model as a function of depth for models with anisotropy constrained to zero for splines below 200 km (Model A), below 700 km (Model B), between 700 and 2400 km (Model C), and between 1200 and 2400 km (Model D).

Figure 14. V_S (A,B) and ξ structure (C,D) at a depth of 2800 km centered under the central Pacific (A,C) and Africa (B,D)

Figure 15. Comparison of ξ structure of SAW24AN16 (A) and the model from Panning & Romanowicz (2004) (B) both truncated at spherical harmonic degree 8.

Figure 16. ξ structure at 2800 km with ϕ and η scaled (A), fixed to that of Boschi & Dziewonski (2000) (B) and inverted independently (C). Note the ξ starting model of the model in (C) was the model shown in (A), while the starting ϕ and η models were defined by Boschi & Dziewonski (2000). The ξ model when topography is allowed on the CMB is also shown (D).

Figure 17. Comparison of Harvard CMT scalar seismic moment (M_0) to the M_0 from the source inversions with unconstrained moment. Solid line represents the case of no bias.

Figure 18. Summed vector shifts for all events in 5° by 5° cells (A), and normalized by the number of events in each cell (B). Note the vectors in (B) are at a different scale than (A).

Figure 19. Resolution matrix checkerboard test for isotropic V_S structure. The input model (column A) produces the output structure in column B, when no anisotropic structure is included in the input, and the model in column C when anisotropic structure is also present in the input model. Numbers in parentheses are the maximum amplitude for each map. The shading is scaled to the maximum amplitude in column A for each depth.

Figure 20. Same as figure 19 for ξ structure. The input model (column A) does not include isotropic structure for the output in column B, but does for column C.

Figure 21. Resolution matrix test where input ξ structure is constrained to a single radial spline. Input amplitude (solid line) and output (dashed line) is shown for splines with peak amplitudes at 121 (A), 321 (B), 621 (C), 996 (D), 1521 (E), 2096 (F) and 2771 km depth (G), as well as at the CMB (H).

Figure 22. Standard error of model values calculated using a bootstrap algorithm at several depths for V_S (A-E) and ξ (F-J). The RMS amplitude of the standard error as a function of depth (K) is also shown for V_S (solid) and ξ (dashed), and can be compared with amplitudes of the model structure shown in Figure 9. Note that the errors are quoted in percent perturbation from the reference model, not as percentages of the final model amplitudes. The color scale is not saturated.

Figure 23. Correlation of V_S (solid) and ξ (dashed) of the final model with the model including isotropic crustal perturbations (A) and topography on the 670 discontinuity and core-mantle boundary (B).

Figure 24. Topography of the CMB (A) and the 670 discontinuity (B). Values are perturbations of the discontinuity radius, so negative values correspond to depressions of the discontinuity, while positive values are elevated regions. The 670 topography displayed does not include the mean positive shift of 6.5 km.

Figure 25. Correlation with the final ξ model as function of depth for a model with ϕ and η structure fixed (solid), and a model with ϕ and η treated as independent parameters in the inversion (dashed). Both models are inverted from data not including source parameters discussed in section 3.6. The starting model for the fixed inversion had no ξ structure. For the independent inversion, the starting model included the ξ structure used for the CMT inversions, as well as a starting ϕ and η model.

Figure 26. Correlation to SAW24AN16 as a function of depth (A) and RMS profiles (B) for V_S (solid) and ξ (dashed) calculated from an inversion for V_{SV} and V_{SH}. Compare to the rms profiles for the preferred model shown in figure 9.

APPENDIX A: ANISOTROPIC SENSITIVITY KERNELS

We parameterize our model in terms of radial anisotropy, which can be described with 5 elastic parameters, most commonly expressed as the Love parameters: A, C, L, N and F (Love 1927). We wish to extend the isotropic kernels from Woodhouse (1980) to an anisotropic medium (e.g. Mochizuki (1986); Romanowicz and Snieder (1988)). It is shown in Appendix C of Li and Romanowicz (1996), that with a model parameterized in spherical harmonics and under the assumption of smooth structure, we can express the frequency shift of coupled modes as

$$\delta\omega_{KK'} = \frac{1}{2\,\omega_{KK'}} \left\{ \sum_{st} \left(\int_0^a [\delta z_{st}]\, r^2\, dr \; - \sum_d r_d^2\, h_d^{st}\, [z_s]_-^+ \right) \right\}, \tag{A1}$$

where s and t refer to the angular and azimuthal order of the spherical harmonics expansion of the model, and

$$\delta z_{st} = \delta A_{st}\bar{A}_s + \delta C_{st}\bar{C}_s + \delta L_{st}\bar{L}_s + \delta N_{st}\bar{N}_s + \delta F_{st}\bar{F}_s + \delta\rho_{st}R_s^{(2)} \tag{A2}$$

and

$$z_s = A\tilde{A}_s + C\tilde{C}_s + L\tilde{L}_s + N\tilde{N}_s + F\tilde{F}_s + \rho R_s^{(1)}. \tag{A3}$$

In (A2), δA_{st}, δC_{st}, δL_{st}, δN_{st}, δF_{st} and $\delta\rho_{st}$ refer to the coefficients in the spherical harmonic expansion of the perturbation of the 5 anisotropic parameters and density. In (A3), A, C, L, N, F and ρ refer to the values of those parameters as a function of depth in the reference model. The kernels $R_s^{(1)}$ and $R_s^{(2)}$ are defined in Woodhouse (1980), and the other kernels, $\bar{A}_s$, $\bar{C}_s$, $\bar{L}_s$, $\bar{N}_s$, $\bar{F}_s$; and $\tilde{A}_s$, $\tilde{C}_s$, $\tilde{L}_s$, $\tilde{N}_s$, $\tilde{F}_s$ are given by

$$\bar{A}_s = Aff'B_{l'sl}^{(0)+} \tag{A4}$$

$$\bar{C}_s = C\dot{U}\dot{U}'B_{l'sl}^{(0)+} \tag{A5}$$

$$\bar{L}_s = L\left((XX'+ZZ')B_{l'sl}^{(1)+} + (ZX'-XZ')iB_{l'sl}^{(1)-}\right) \tag{A6}$$

$$\bar{N}_s = N\left(-ff'B_{l'sl}^{(0)+} + \frac{1}{r^2}(VV'+WW')B_{l'sl}^{(2)+} + \frac{1}{r^2}(WV'-VW')iB_{l'sl}^{(2)-}\right) \tag{A7}$$

$$\bar{F}_s = F(\dot{U}f'+\dot{U}'f)B_{l'sl}^{(0)+} \tag{A8}$$

$$\tilde{A}_s = ff'B_{l'sl}^{(0)+} \tag{A9}$$

$$\tilde{C}_s = -\dot{U}\dot{U}'B_{l'sl}^{(0)+} + \frac{1}{r}(V\dot{U}'B_{ll's}^{(1)+} + V'\dot{U}B_{l'ls}^{(1)+}) + \frac{1}{r}(\dot{U}W'-\dot{U}'W)iB_{l'sl}^{(1)-}) \tag{A10}$$

$$\tilde{L}_s = (XX' + ZZ' - \dot{V}X' - \dot{V}'X - \dot{W}Z' - \dot{W}'Z)B^{(1)+}_{l'sl}$$
$$+(ZX' + XZ' - \dot{V}Z' - \dot{V}'Z - \dot{W}X' - \dot{W}'X)iB^{(1)-}_{l'sl} \quad \text{(A11)}$$

$$\tilde{N}_s = -ff'B^{(0)+}_{l'sl} + \frac{1}{r^2}(VV' + WW')B^{(2)+}_{l'sl} + \frac{1}{r^2}(WV' - VW')iB^{(2)-}_{l'sl} \quad \text{(A12)}$$

$$\tilde{F}_s = \frac{1}{r}(Vf'B^{(1)+}_{ll's} + V'fB^{(1)+}_{l'ls}) + \frac{1}{r}(fW' - Wf')iB^{(1)-}_{l'sl} \quad \text{(A13)}$$

with

$$f = \frac{1}{r}[2U - l(l+1)V] \quad \text{(A14)}$$

$$X = \dot{V} + \frac{1}{r}(U - V) \quad \text{(A15)}$$

$$Z = \dot{W} - \frac{1}{r}W \quad \text{(A16)}$$

and

$$B^{(N)\pm}_{l'sl} = \frac{1}{2}(1 \pm (-1)^{l'+s+l}) \left[\frac{(l'+N)!(l+N)!}{(l'-N)!(l-N)!}\right]^{1/2} (-1)^N \begin{pmatrix} l' & s & l \\ -N & 0 & N \end{pmatrix}, \quad \text{(A17)}$$

where

$$\begin{pmatrix} l' & s & l \\ -N & 0 & N \end{pmatrix}$$

is in Wigner $3-j$ notation (Edmonds 1960). U, V and W are the radial eigenfunctions of each mode, and the primes refer to the properties of the second mode in each coupled pair. Note that (A4)-(A8) differ from equations C4-C8 in Li and Romanowicz (1996), as we assume here that the model perturbations are relative, dimensionless perturbations (i.e. δA_{st} refers to the coefficient in the spherical harmonic expansion of $\delta \ln A$) rather than absolute perturbations of the elastic values.

We wish to reparameterize in terms of Voight average V_P and V_S, and the three anisotropic parameters ξ, ϕ and η. We use this parameterization due to practical concerns of the inversion process. In general, given sufficient coverage, an iterative least-squares inversion, such as the approach we use in our modelling (Tarantola & Valette 1982) has better resolution of the 3D pattern of structure than the amplitude of that structure, due to the *a priori* damping scheme applied. If we choose a parameterization such as the Love coefficients, the anisotropy, which is the quantity we are interested in, is defined by the differences between inverted parameters. Interpreting the

difference of two terms with uncertainties in amplitude from the damping procedure is very problematic both in terms of amplitude and even sign, so we choose to invert directly for the anisotropic parameters.

To define the Voight average equivalent isotropic velocities, we start from the definition of the equivalent Voight average bulk and shear moduli in a radially anisotropic medium (Babuska & Cara 1991),

$$\kappa = \frac{1}{9}(C + 4A - 4N + 4F) \tag{A18}$$

$$\mu = \frac{1}{15}(C + A + 6L + 5N - 2F). \tag{A19}$$

The isotropic velocities are defined in terms of the bulk and shear moduli,

$$V_P^2 = \frac{\kappa + \frac{4}{3}\mu}{\rho} \tag{A20}$$

$$V_S^2 = \frac{\mu}{\rho}, \tag{A21}$$

and so we can substitute (A18) and (A19) into (A20) and (A21) to obtain

$$\rho {V_P}^2 = \frac{1}{15}(3C + (8 + 4\eta)A + 8(1 - \eta)L) \tag{A22}$$

$$\rho {V_S}^2 = \frac{1}{15}(C + (1 - 2\eta)A + (6 + 4\eta)L + 5N), \tag{A23}$$

where

$$\eta = \frac{F}{A - 2L}, \tag{A24}$$

which is equal to 1 in an isotropic model, and effectively describes anisotropy in the Lamé parameter λ. The relationships between the Love coefficients and observable seismic velocities are defined in equations (1)-(4).

Note that the average isotropic velocities defined in (A22) and (A23) depend on all four of the observable seismic velocities in (1)-(4), as well as η. However, in the case of small anisotropy which we assume for our perturbation-based approach, we can assume $\eta \simeq 1$, and make the first order approximation to neglect the quantity $C - A$ in comparison with $10L + 5N$ in (A23), and simplify the Voight average velocities to

$$V_S^2 = \frac{2L + N}{3\rho} = \frac{2V_{SV}^2 + V_{SH}^2}{3} \tag{A25}$$

$$V_P^2 = \frac{C+4A}{5\rho} = \frac{V_{PV}^2 + 4V_{PH}^2}{5}, \tag{A26}$$

such that the average isotropic S velocity depends only on V_{SV} and V_{SH}, and the P velocity only depends on V_{PV} and V_{PH}.

Taking the isotropic velocities and the anisotropic parameters ξ, ϕ, and η defined in equations (8)-(10) and obtain the differentials,

$$\delta \ln V_S = \frac{2\delta L + \delta N}{4L+2N} - \frac{1}{2}\delta \ln \rho \tag{A27}$$

$$\delta \ln V_P = \frac{\delta C + 4\delta A}{2C+8A} - \frac{1}{2}\delta \ln \rho \tag{A28}$$

$$\delta \ln \xi = \delta \ln N - \delta \ln L \tag{A29}$$

$$\delta \ln \phi = \delta \ln C - \delta \ln A \tag{A30}$$

$$\delta \ln \eta = \delta \ln F - \frac{\delta A - 2\delta L}{A-2L}. \tag{A31}$$

The sensitivity kernels for the desired parameterization will be linear combinations of the kernels described in (A4)-(A8). For convenience, we will drop the subscripts pertaining to the spherical harmonic expansion coefficients, and describe the kernel conversion in more general terms. Since we are no longer assuming a spherical harmonic expansion, we will refer to the general kernel for a relative shift in a model parameter (i.e. K_A would be the kernel describing the frequency shift due to a relative perturbation, $\delta \ln A$). Because an equivalent model perturbation should produce the same shift in mode frequency for any parameterization, we substitute equations (A27)-(A31) into

$$\begin{aligned} &K_A\delta \ln A + K_C\delta \ln C + K_L\delta \ln L + K_N\delta \ln N + K_F\delta \ln F + K_\rho^{(1)}\delta \ln \rho \\ &\quad = K_{V_S}\delta \ln V_S + K_{V_P}\delta \ln V_P + K_\xi\delta \ln \xi + K_\phi\delta \ln \phi + K_\eta\delta \ln \eta + K_\rho^{(2)}\delta \ln \rho \end{aligned} \tag{A32}$$

where $K_\rho^{(1)}$ refers to the density kernel for the parameterization as in Li and Romanowicz (1996), and $K_\rho^{(2)}$ is the kernel for the new parameterization, which will be different due to the inclusion of density sensitivity inside the velocity terms. Solving for the new kernels, we get

$$K_{V_S} = 2(K_L + K_N - \frac{2L}{A-2L}K_F) \tag{A33}$$

$$K_{V_P} = 2(K_A + K_C + \frac{A}{A-2L}K_F) \tag{A34}$$

$$K_\xi = \frac{1}{2L+N}(2LK_N - NK_L + \frac{2LN}{A-2L}K_F) \tag{A35}$$

$$K_\phi = \frac{1}{C+4A}(4AK_C - CK_A - \frac{AC}{A-2L}K_F) \tag{A36}$$

$$K_\eta = K_F \tag{A37}$$

$$K_\rho^{(2)} = K_\rho^{(1)} + K_A + K_C + K_L + K_N + K_F. \tag{A38}$$

APPENDIX B: AUTOMATIC WAVEPACKET PICKING ALGORITHM

The early models developed using *NACT* (Li & Romanowicz 1995), were constructed using only transverse (T) component data (Li & Romanowicz 1996; Mégnin & Romanowicz 2000), the component of horizontal motion perpendicular to the great circle path between source and receiver. Because of the relative simplicity of these waveforms, the wavepackets used in these inversions were picked by hand. Because there is no coupling with P energy, the body wave phases are, in general, well isolated, allowing for quick visual assessment of data quality and definition of wavepacket windows utilizing an interactive approach.

To develop anisotropic models we need wavepackets from all three components. The longitudinal (L) component (horizontal motion parallel with the great circle path) and vertical (Z) component of motion measure motion of the coupled P-SV system. There are many more body wave phases on these records, as we have P phases, as well as P to S conversions such as phases that travel through the fluid outer core, and conversions at the free surface and mantle discontinuities, which are not present on the T component. Picking isolated wavepackets is very difficult, and the definition of wavepacket windows to maximize sensitivity can be a very time-consuming task if done by hand.

In order to gather a sufficient dataset of L and Z component body waveform data, we developed an automatic wavepacket picking algorithm to speed acquisition, although we review each wavepacket visually to insure data quality.

The dataset includes events from 1995 to 1999 recorded on the IRIS and GEOSCOPE networks. We use events with M_W greater than 5.5, but do not use events with seismic moment greater

than 10^{20} Nm ($M_W > 7.3$) in order to avoid complications from long source-time functions. We also do not use traces within 15° of the source or the antipode, as the asymptotic calculations break down in these regions. All traces matching these criteria are then filtered to the frequency band used in the inversions. For the body waves, the short period cutoff is 32 s at present, while the long period cutoff is a function of the earthquake magnitude and ranges from 220 seconds to 1 hour.

Each trace is then processed to select the wavepackets to be used in the inversion. First synthetics are calculated using the PREM model (Dziewonski & Anderson 1981). We define the two quantities

$$RMSR = \frac{\sum_{i=1}^{N}(d_i - s_i)\cdot(d_i - s_i)}{\sum_{i=1}^{N} d_i^2} \tag{B1}$$

$$RMSS = \frac{\sum_{i=1}^{N}(d_i - s_i)\cdot(d_i - s_i)}{\sum_{i=1}^{N} s_i^2}, \tag{B2}$$

where N is the number of data points, d_i is the ith data point, and s_i is the ith point in the synthetic trace. Data which has either of these values too large is rejected, as it is either noisy, has an incorrect instrument response, contains glitches, or is strongly affected by focussing or defocussing which we do not model in our theoretical approach.

Traces are then divided into wavepackets based on the predicted travel times of several phases. Wavepackets are mostly defined in the window starting just before the predicted first arrival (P, P_{diff}, or PKP) and ending just before the Rayleigh wave. For events deeper than 200 km and epicentral distances between 40° and 90°, we also pick wavepackets in a window beginning after the Rayleigh wave and extending to after the predicted arrival of ScS4, which contains multiple ScS phases in the reverberative interval (Revenaugh & Jordan 1987) between the 1st and 2nd orbit Rayleigh waves.

After the wavepacket windows are defined, each packet is analyzed for data quality, using a number of criteria. First, we calculate the $RMSR$ and $RMSS$ values, and reject packets if either value is greater than 4.0. We also calculate the ratio of maximum data and synthetic amplitudes, and reject the wavepacket if this value is greater than 2.5 or less than 0.4. A correlation coefficient is also calculated, and data is rejected if it is less than 0. Finally the packet is analyzed using a moving window approach which helps eliminate data with persistent low level noise. The $RMSR$

and $RMSS$ values for each packet are stored, and are utilized in the *a priori* data covariance matrix (Tarantola & Valette 1982), which is used to apply a weighting scheme to account for data noise and redundancy (Li & Romanowicz 1996).

This data selection process eliminates approximately 50% of the available data, and stricter criteria can be applied on the $RMSR$ and $RMSS$ values at the time of inversion, if desired. This scheme allows us to gather data much more quickly, although we do review each packet visually to verify its quality. A similar algorithm is used for the picking of surface wavepackets (Gung 2003).

Figure 1

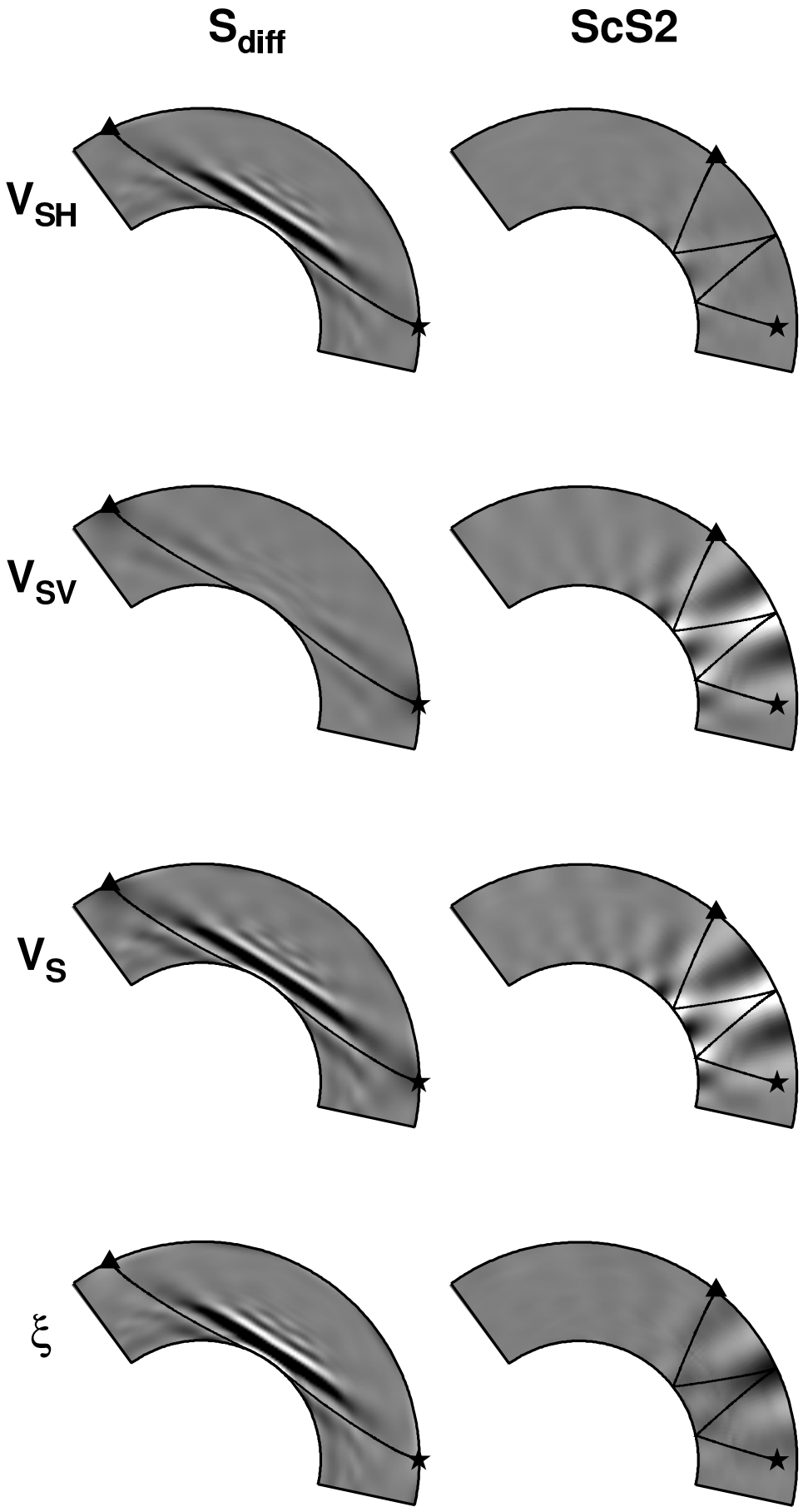

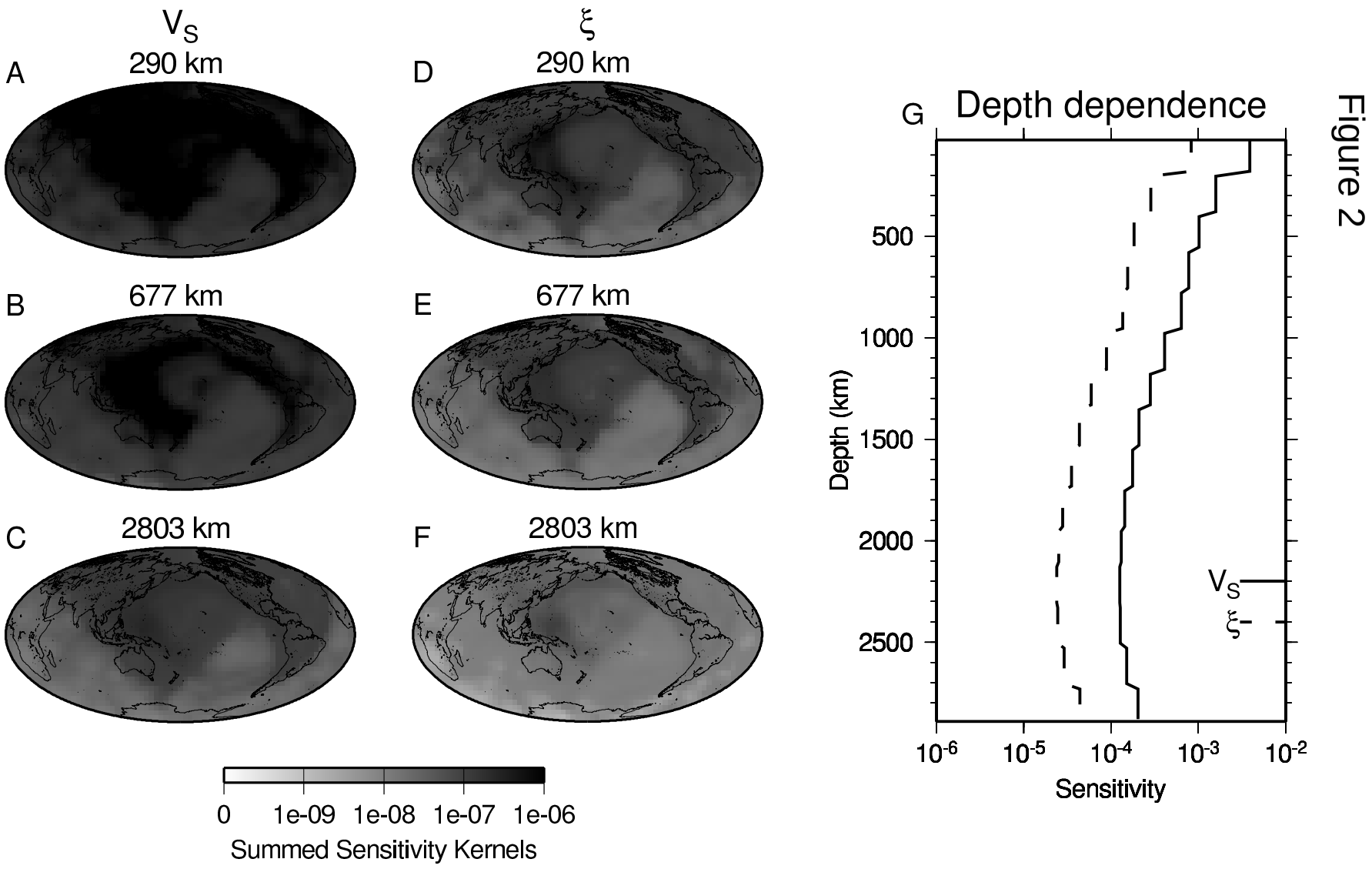
V_S
A
290 km
B
677 km
C
2803 km
ξ
D
290 km
E
677 km
F
2803 km
0
1e-09
1e-08
1e-07
1e-06
Summed Sensitivity Kernels
G
Depth dependence
Depth (km)
500
1000
1500
2000
2500
10^{-6}
10^{-5}
10^{-4}
10^{-3}
10^{-2}
Sensitivity
V_S
ξ

Figure 2

Figure 3

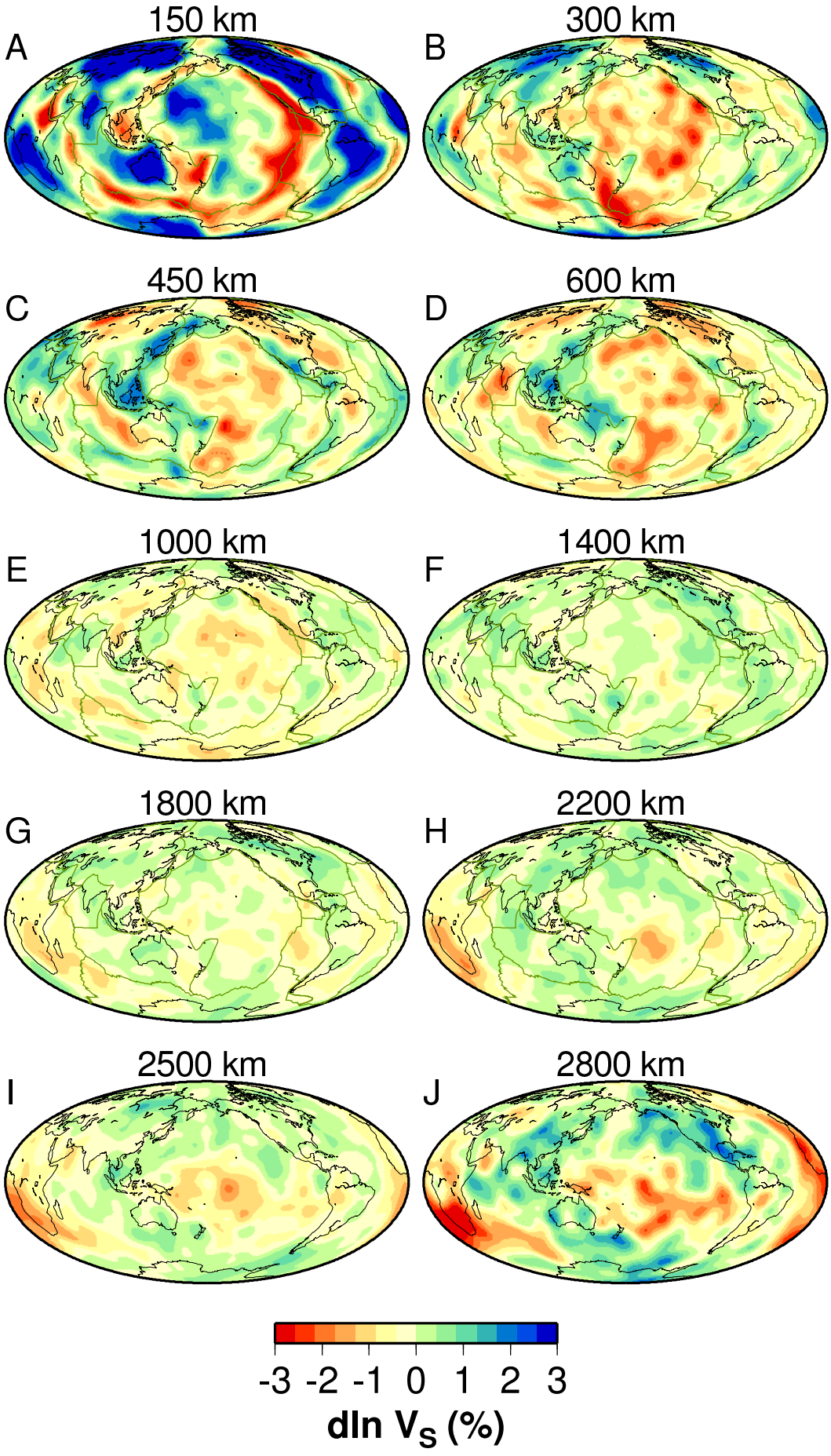
150 km
A
300 km
B
450 km
C
600 km
D
1000 km
E
1400 km
F
1800 km
G
2200 km
H
2500 km
I
2800 km
J
-3 -2 -1 0 1 2 3
dln V_S (%)

Figure 4

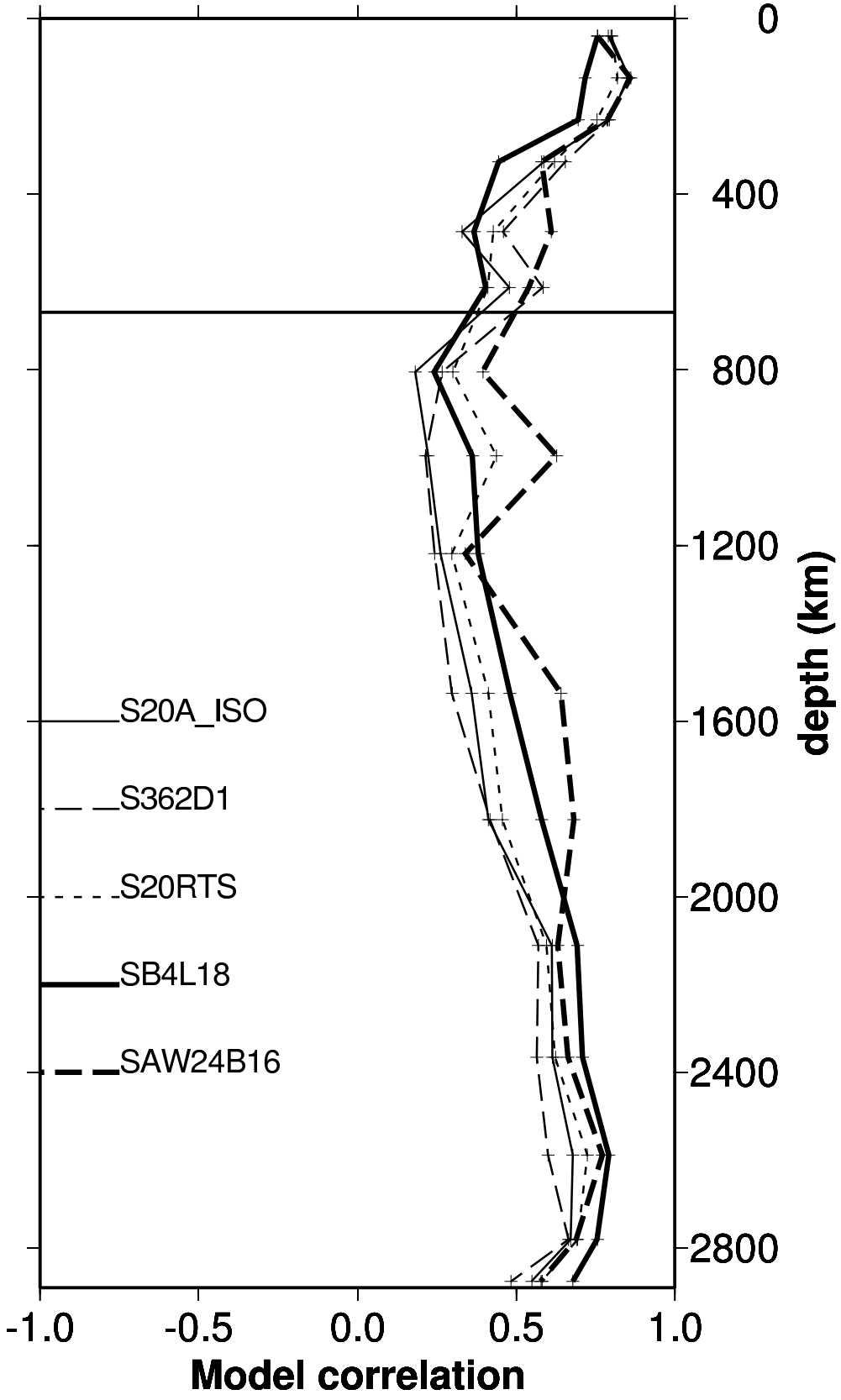
0
400
800
1200
1600
2000
2400
2800
depth (km)
S20A_ISO
S362D1
S20RTS
SB4L18
SAW24B16
-1.0
-0.5
0.0
0.5
1.0
Model correlation

Figure 5

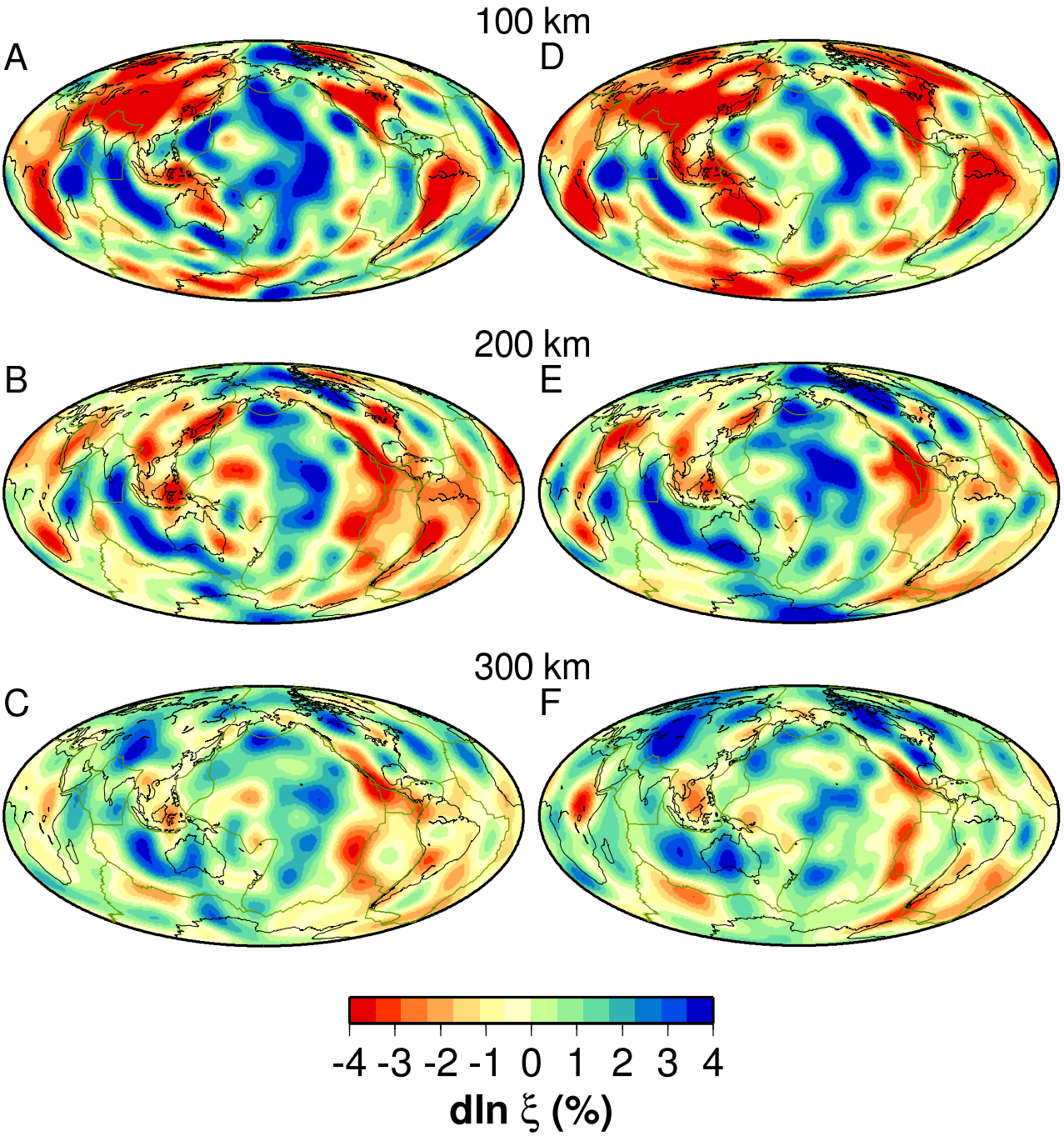

Figure 6

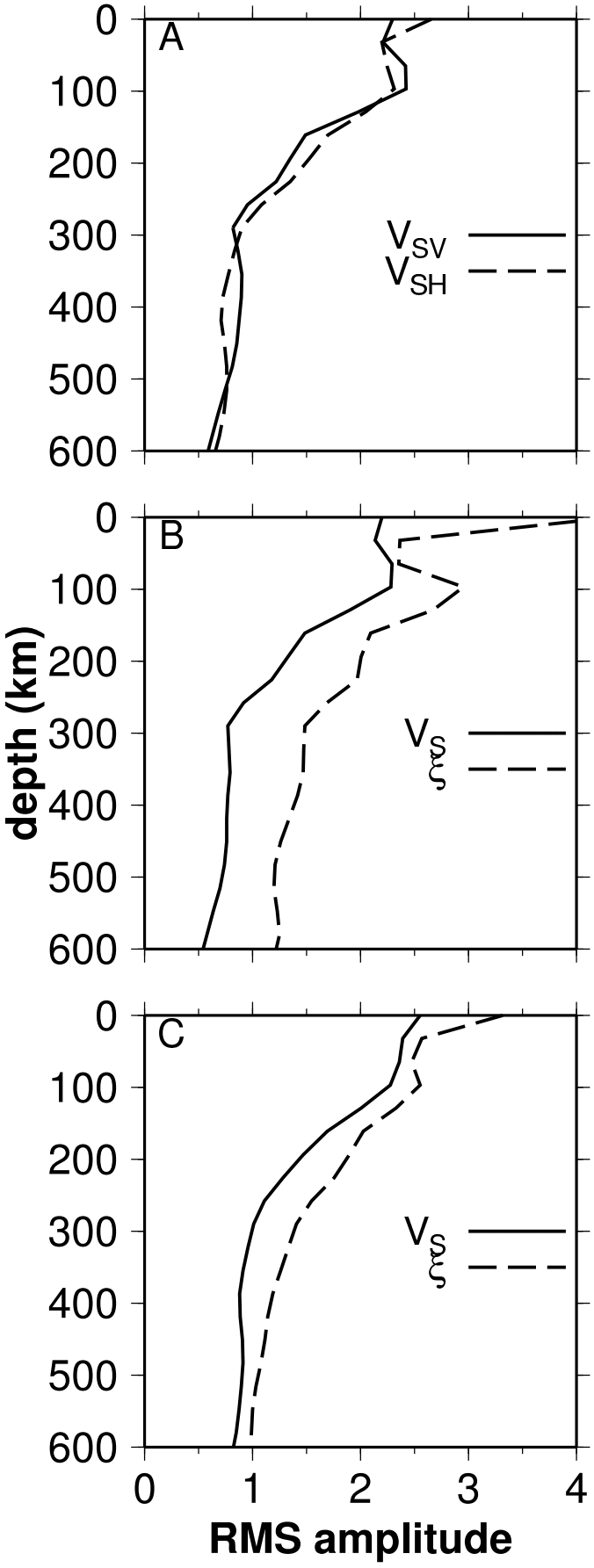
A
B
C
0
100
200
300
400
500
600
depth (km)
V_{SV}
V_{SH}
V_S
V_S
0
1
2
3
4
RMS amplitude

Figure 7

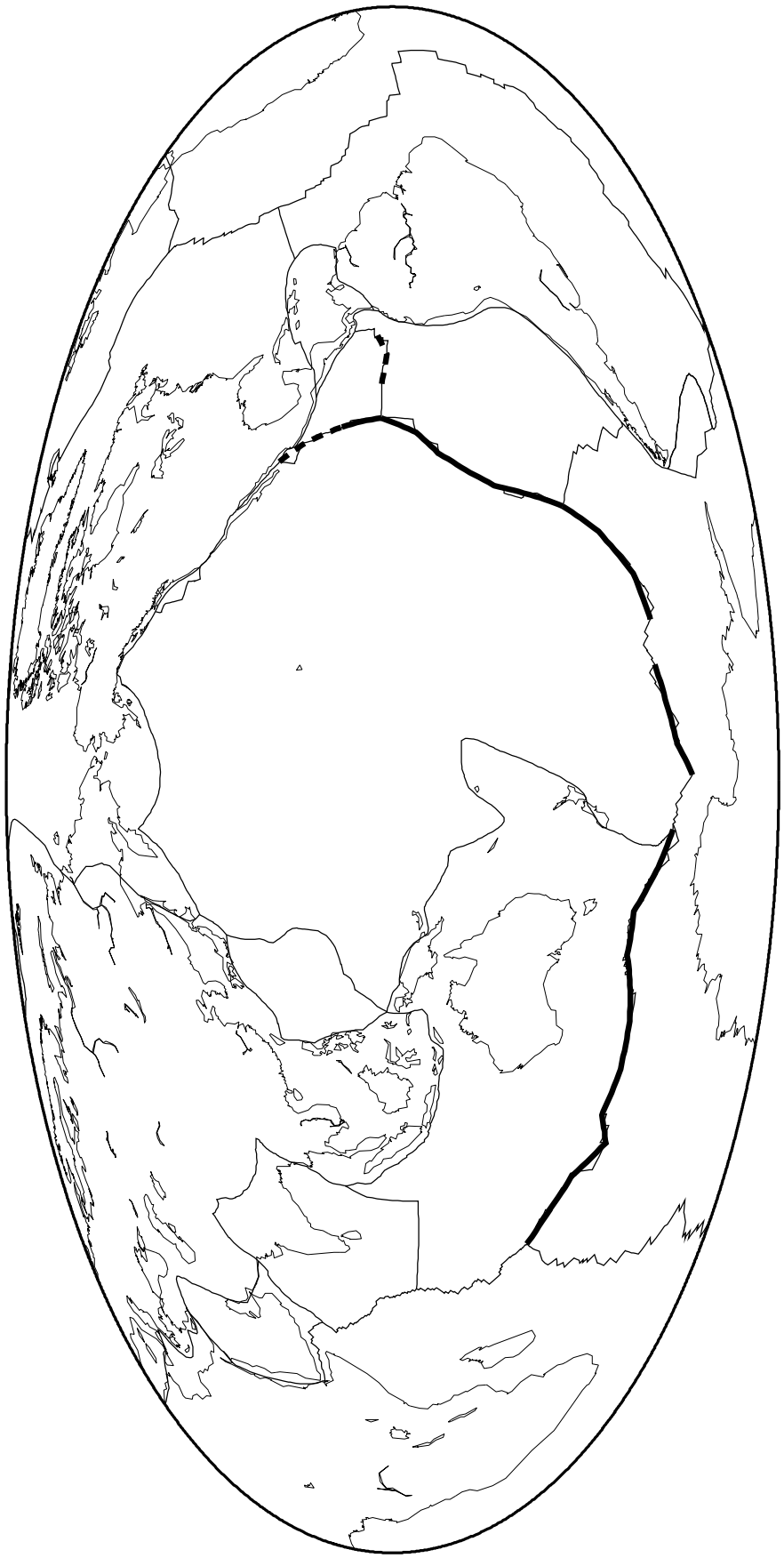

Figure 8

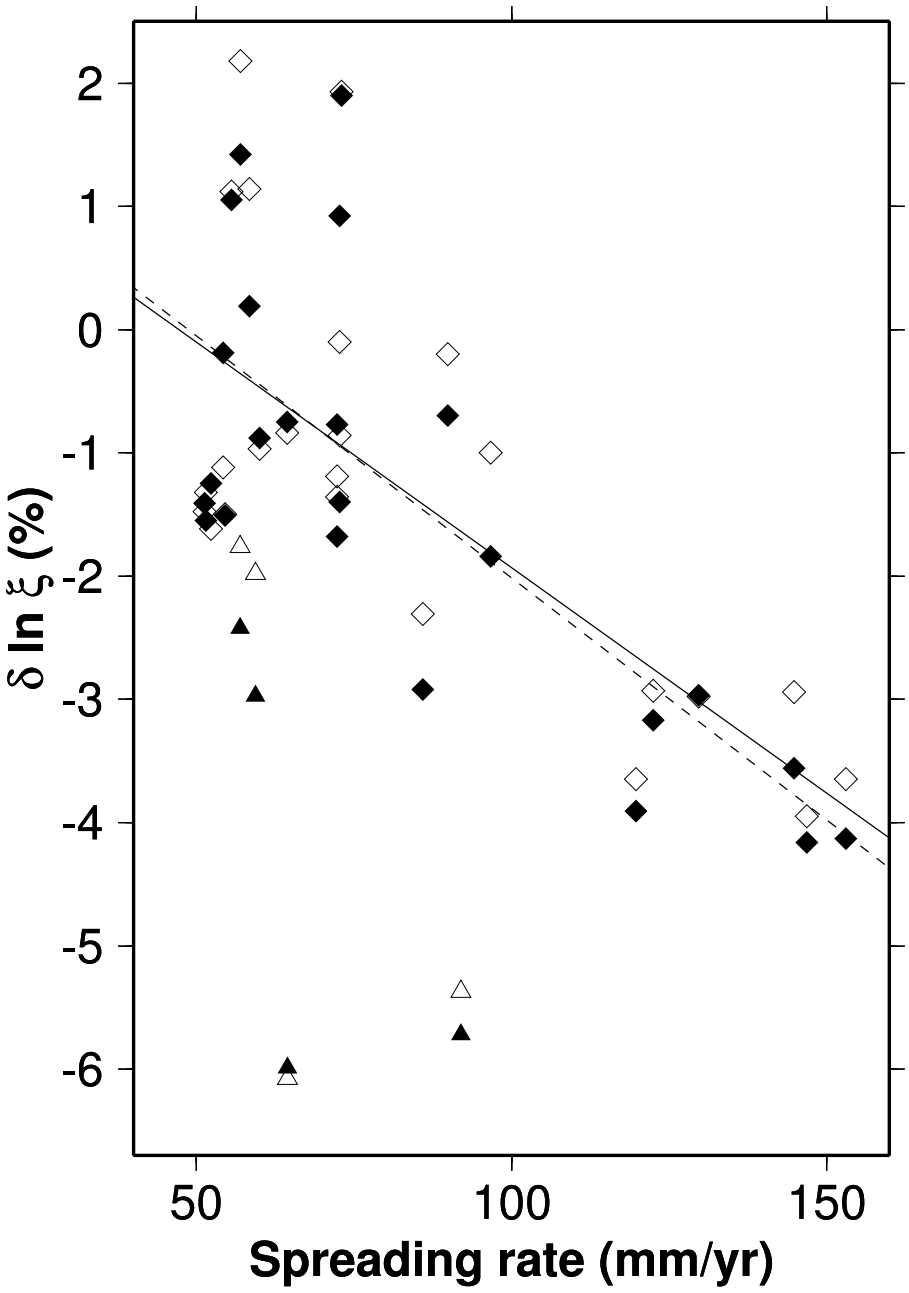

Figure 9

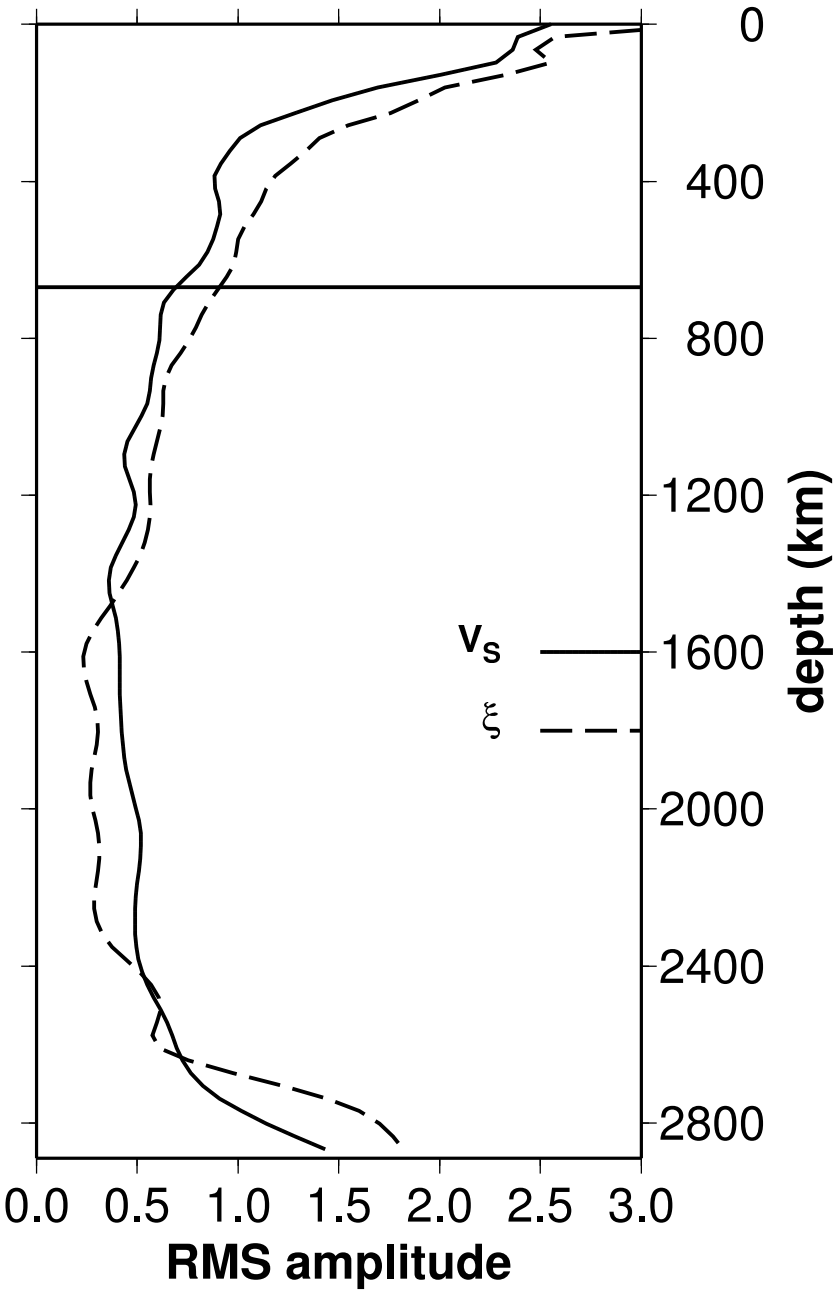
0
400
800
1200
1600
2000
2400
2800
depth (km)
v_S
ξ
0.0 0.5 1.0 1.5 2.0 2.5 3.0
RMS amplitude

Figure 10

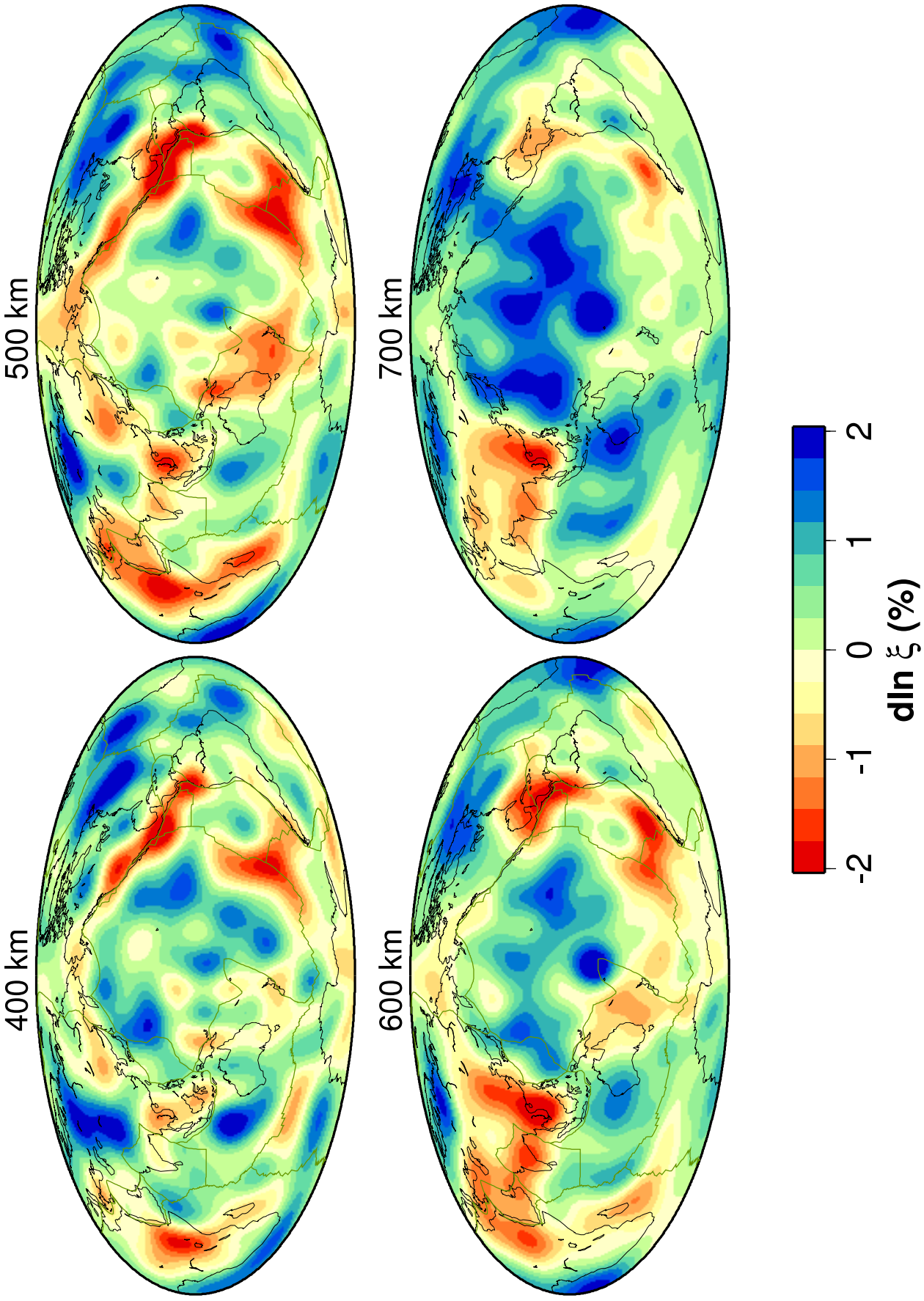

Figure 11

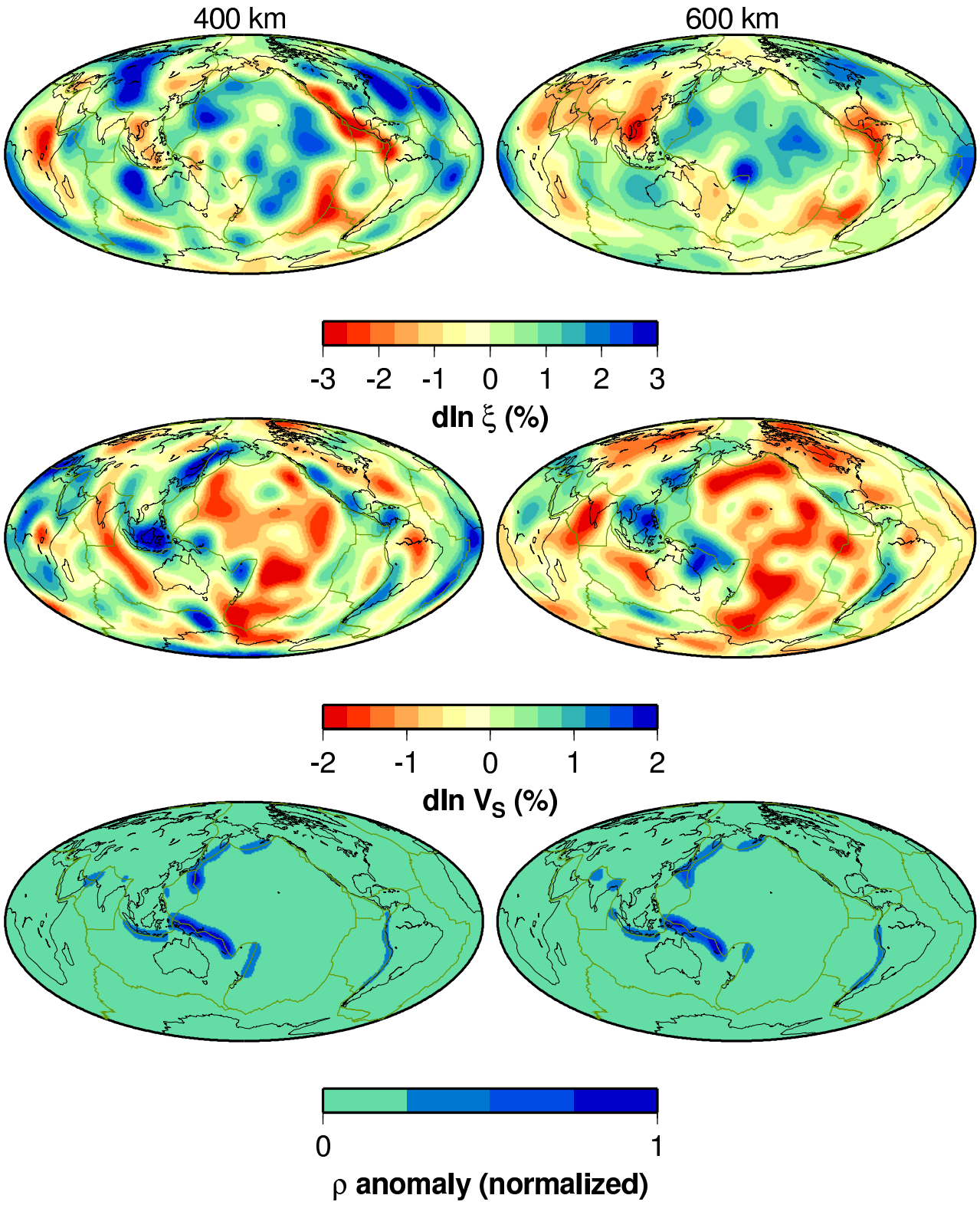
400 km
600 km
-3 -2 -1 0 1 2 3
dln ξ (%)
-2 -1 0 1 2
dln V_S (%)
0 1
ρ anomaly (normalized)

Figure 12

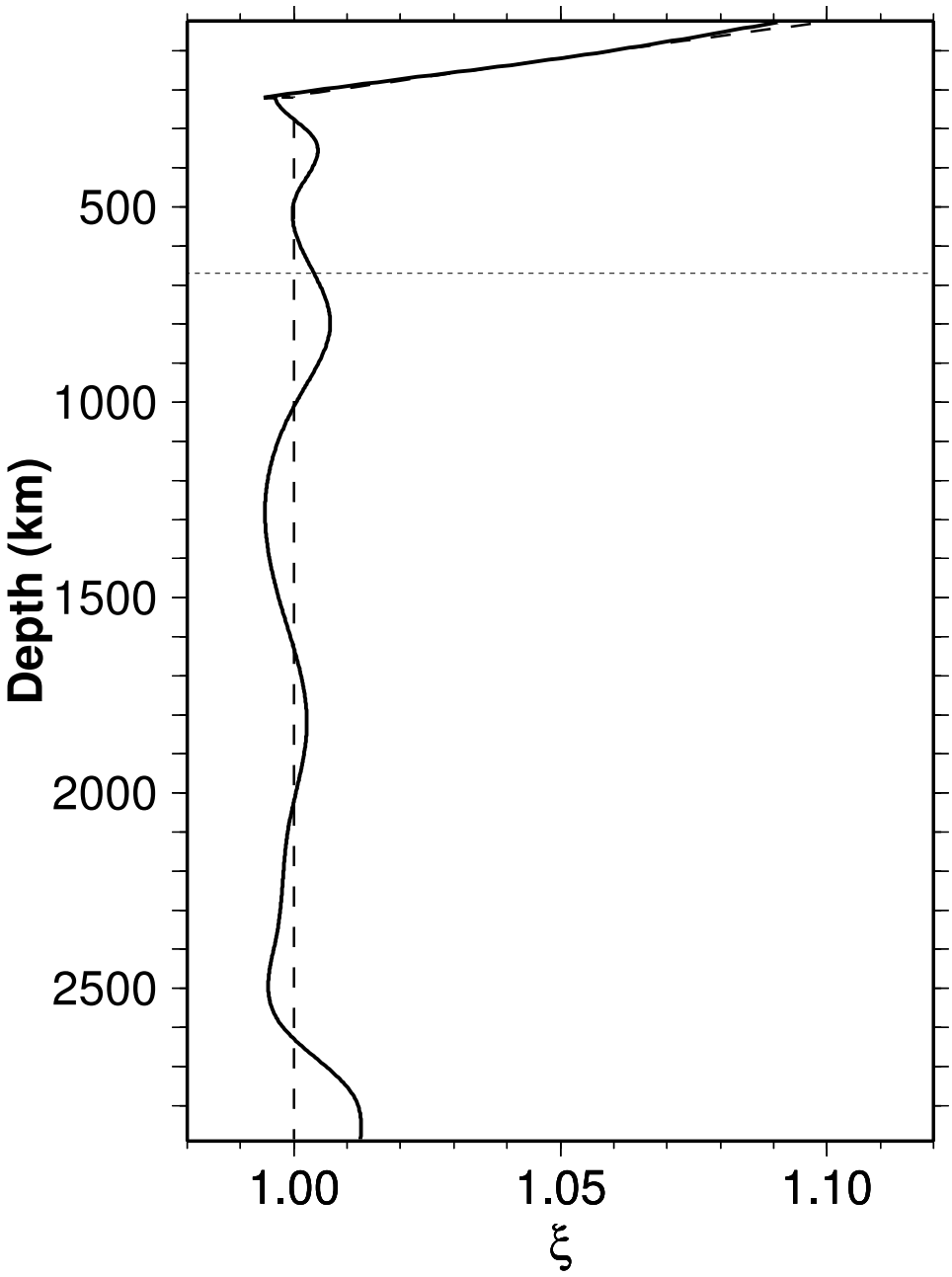

Figure 13

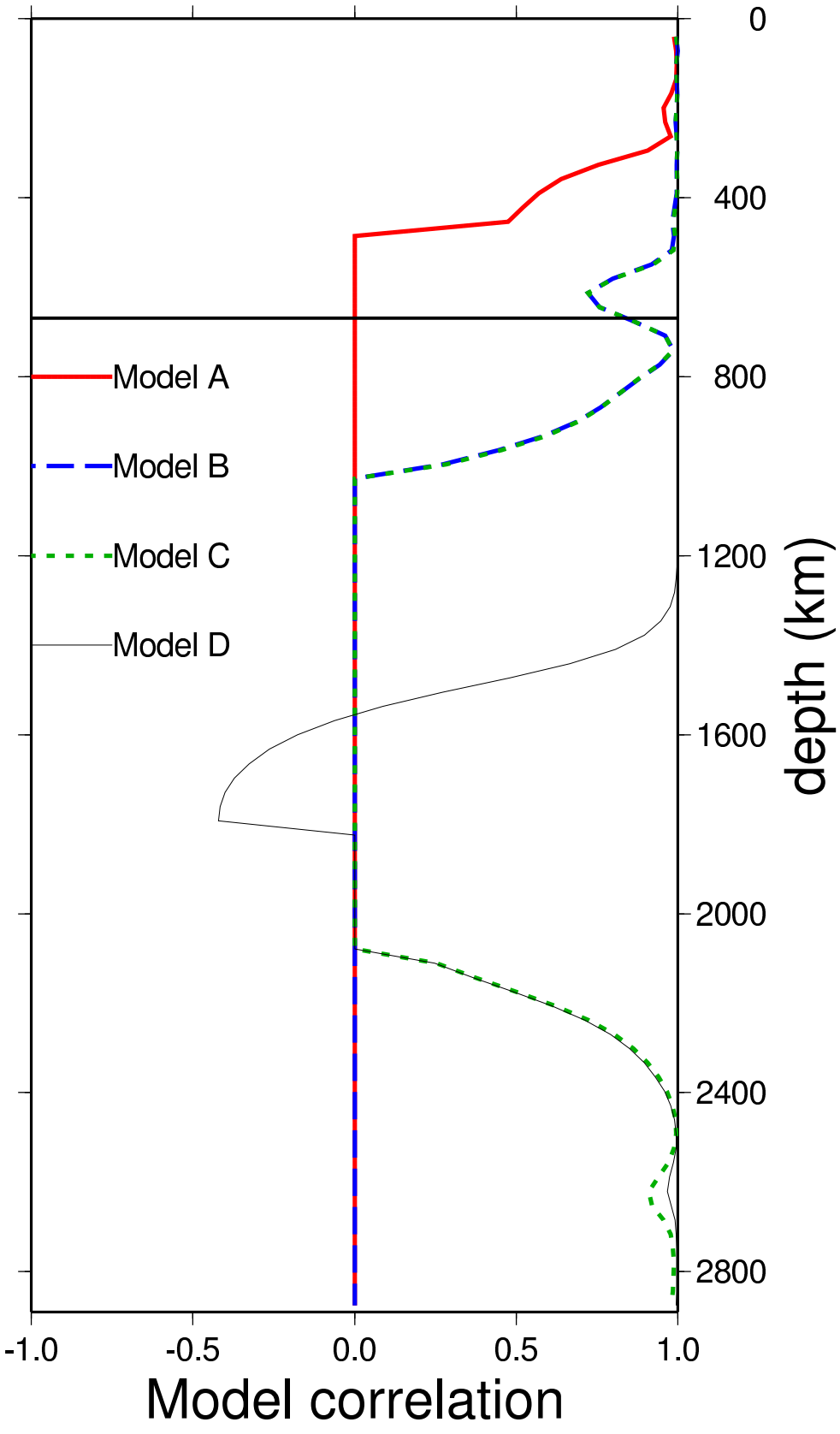
Model A
Model B
Model C
Model D
0
400
800
1200
1600
2000
2400
2800
depth (km)
-1.0
-0.5
0.0
0.5
1.0
Model correlation

Figure 14

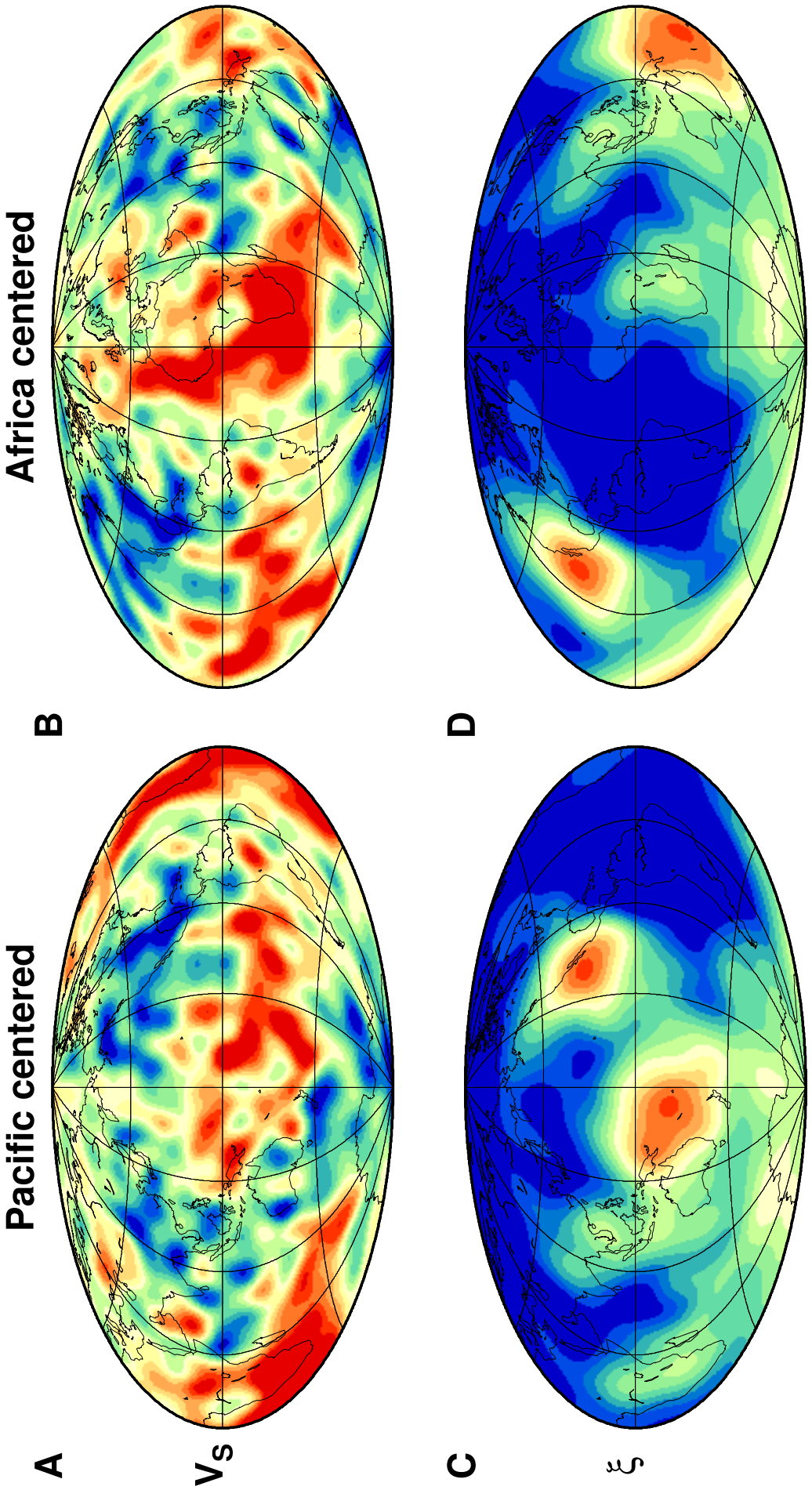
Pacific centered
Africa centered
A
B
C
D
V_S
ξ
-2.0 -1.5 -1.0 -0.5 0.0 0.5 1.0 1.5 2.0
dln(V_S or ξ)(%)

Figure 15

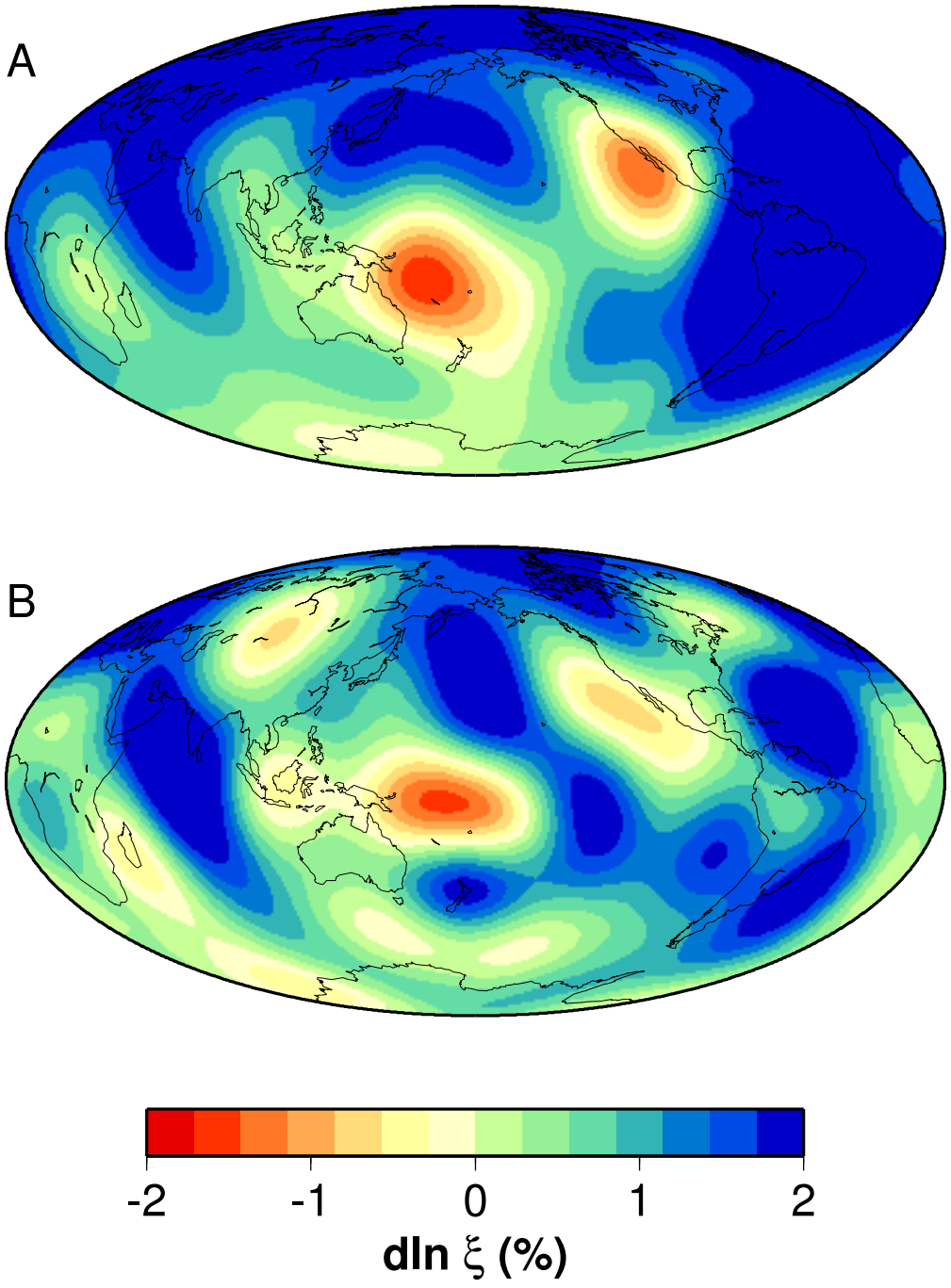

Figure 16

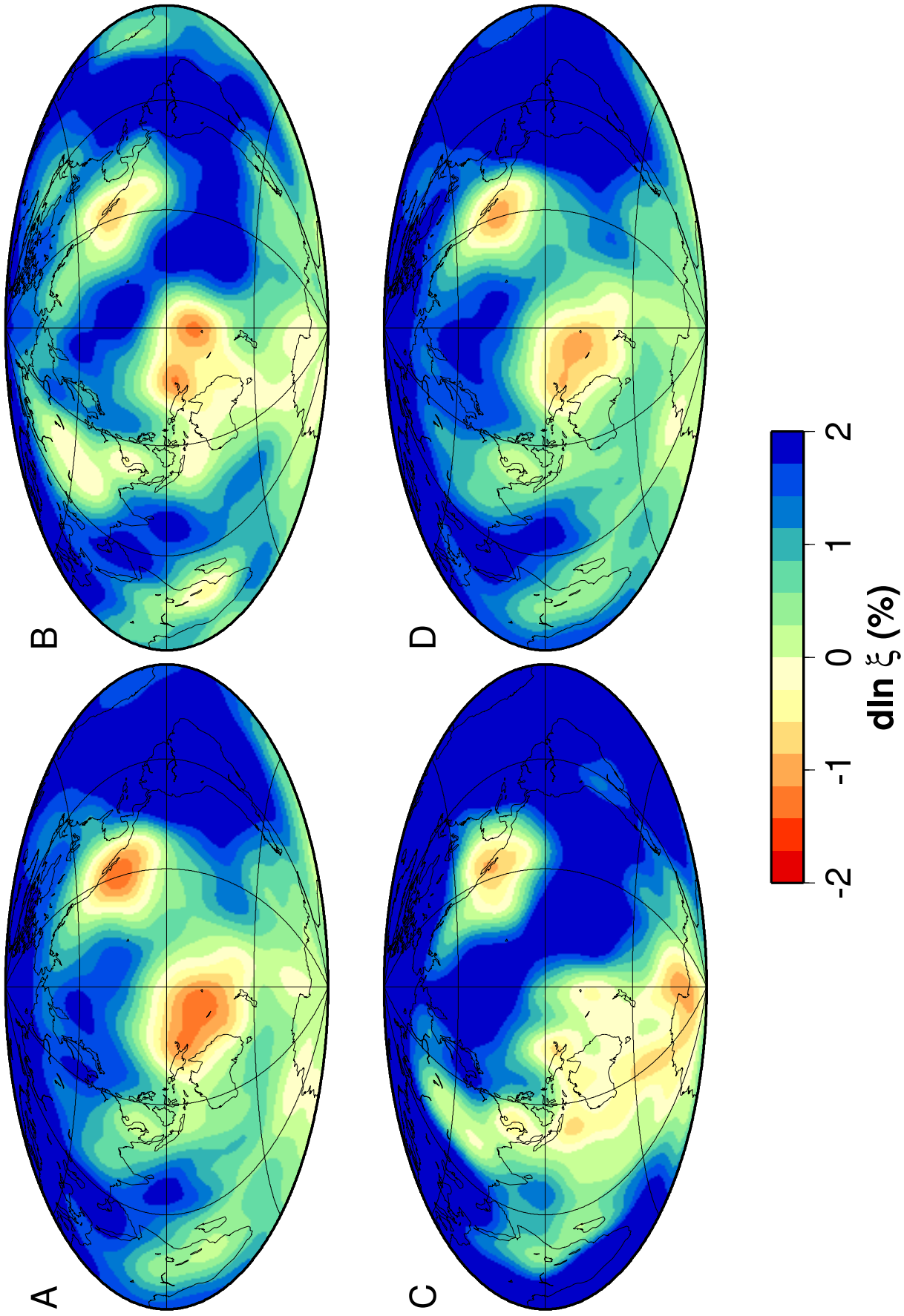

Figure 17

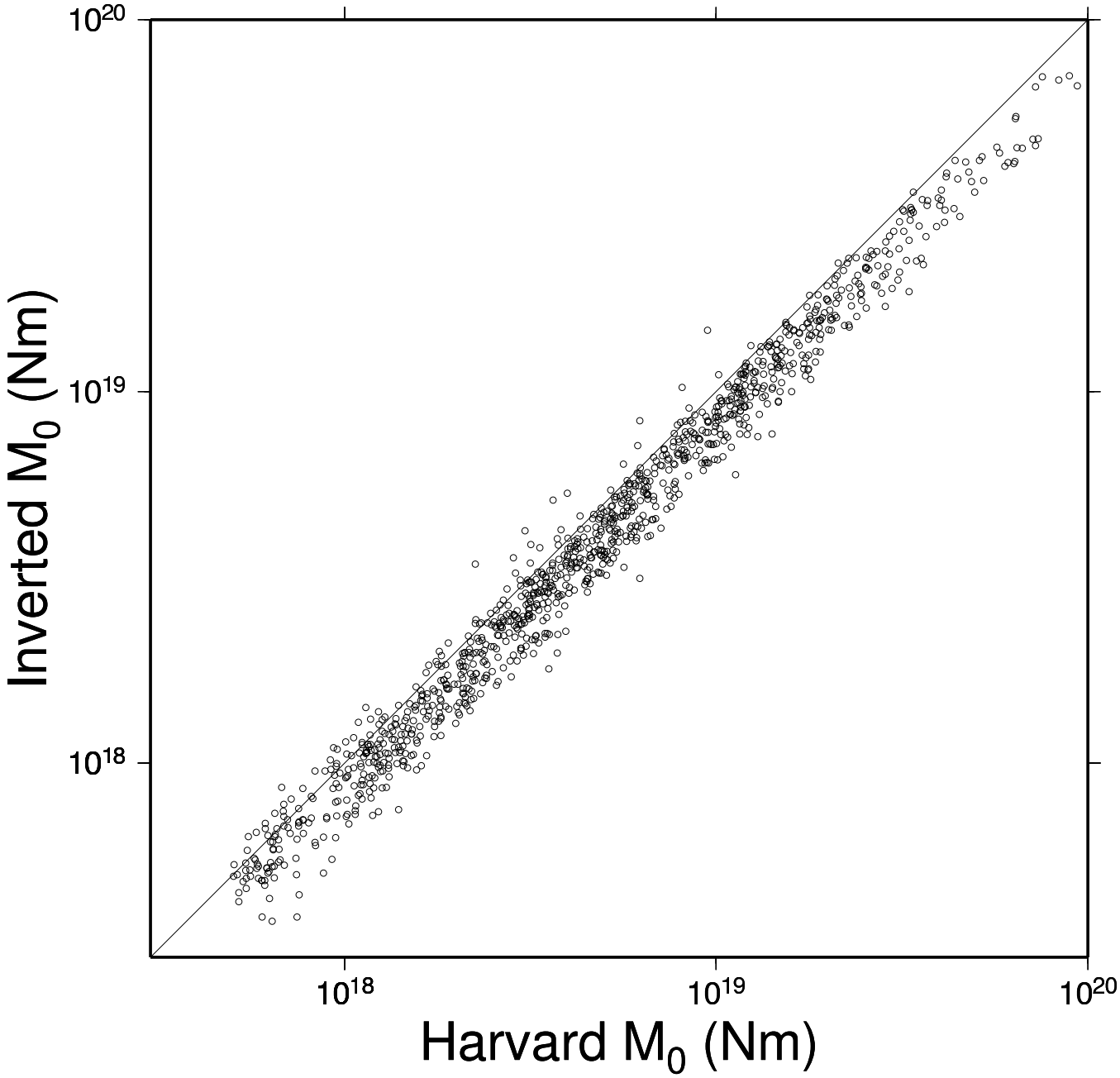

Figure 18

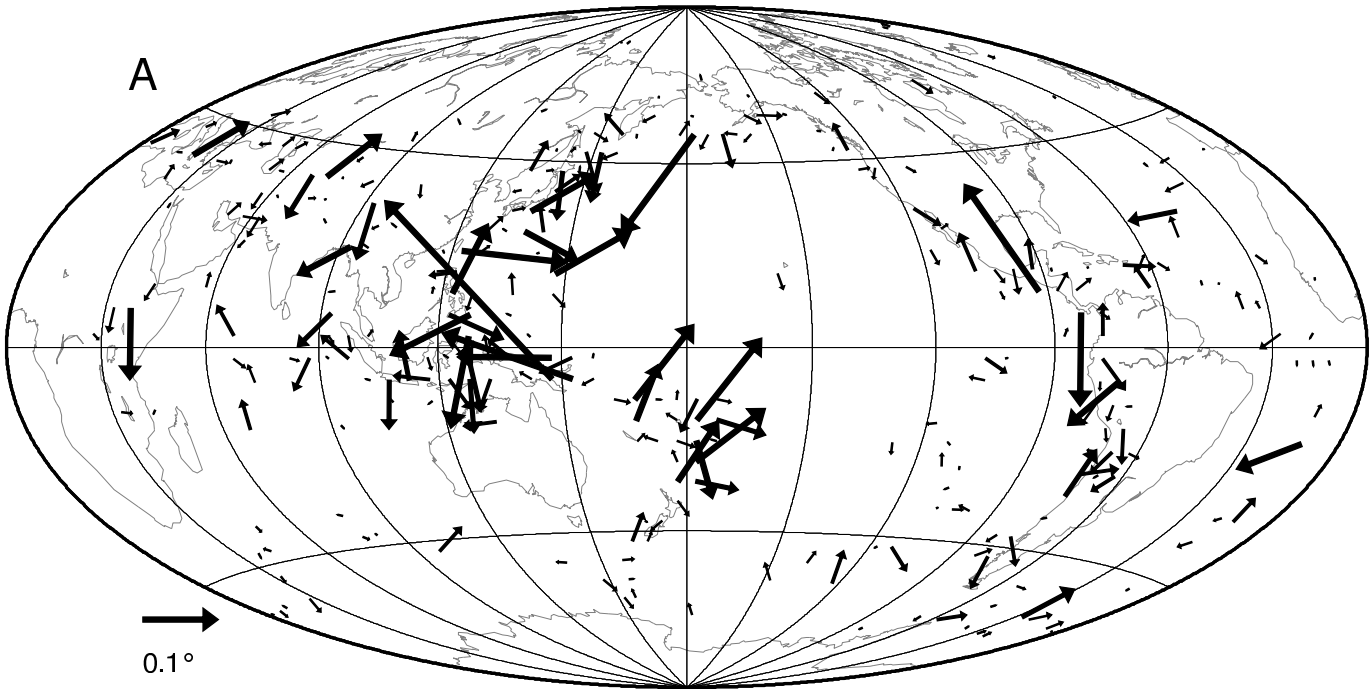

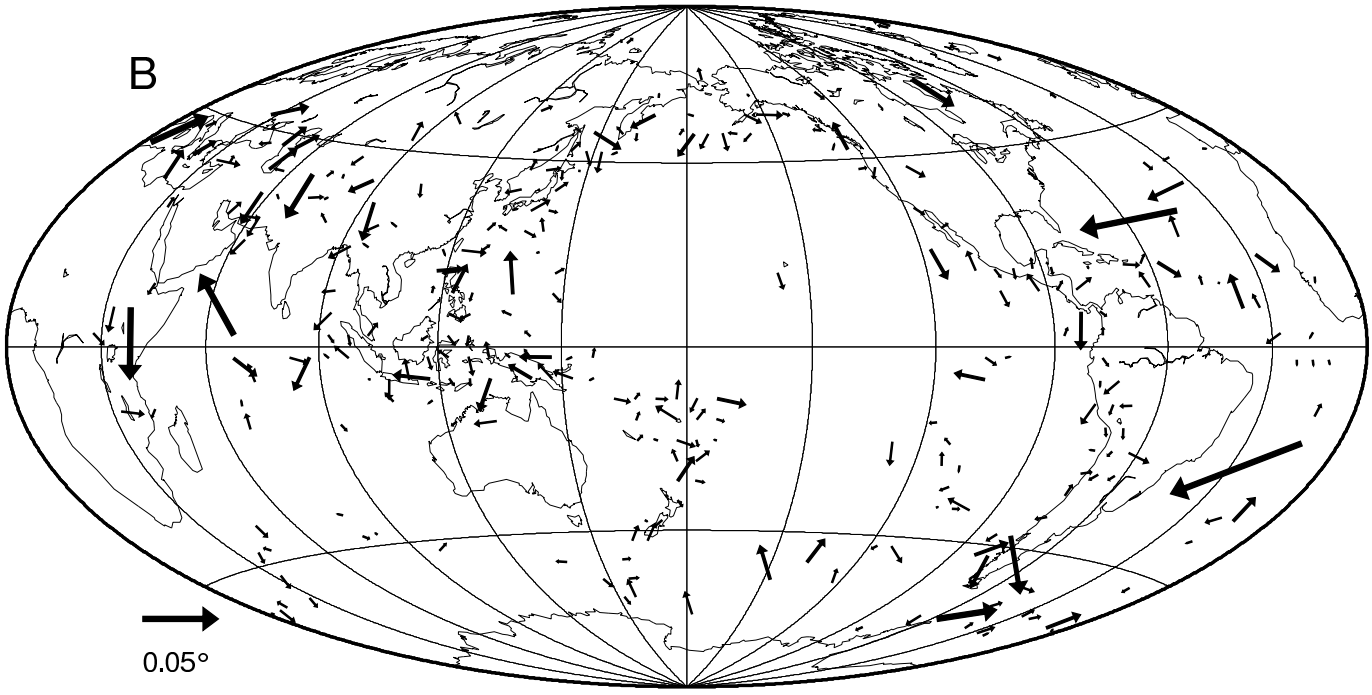

Figure 19

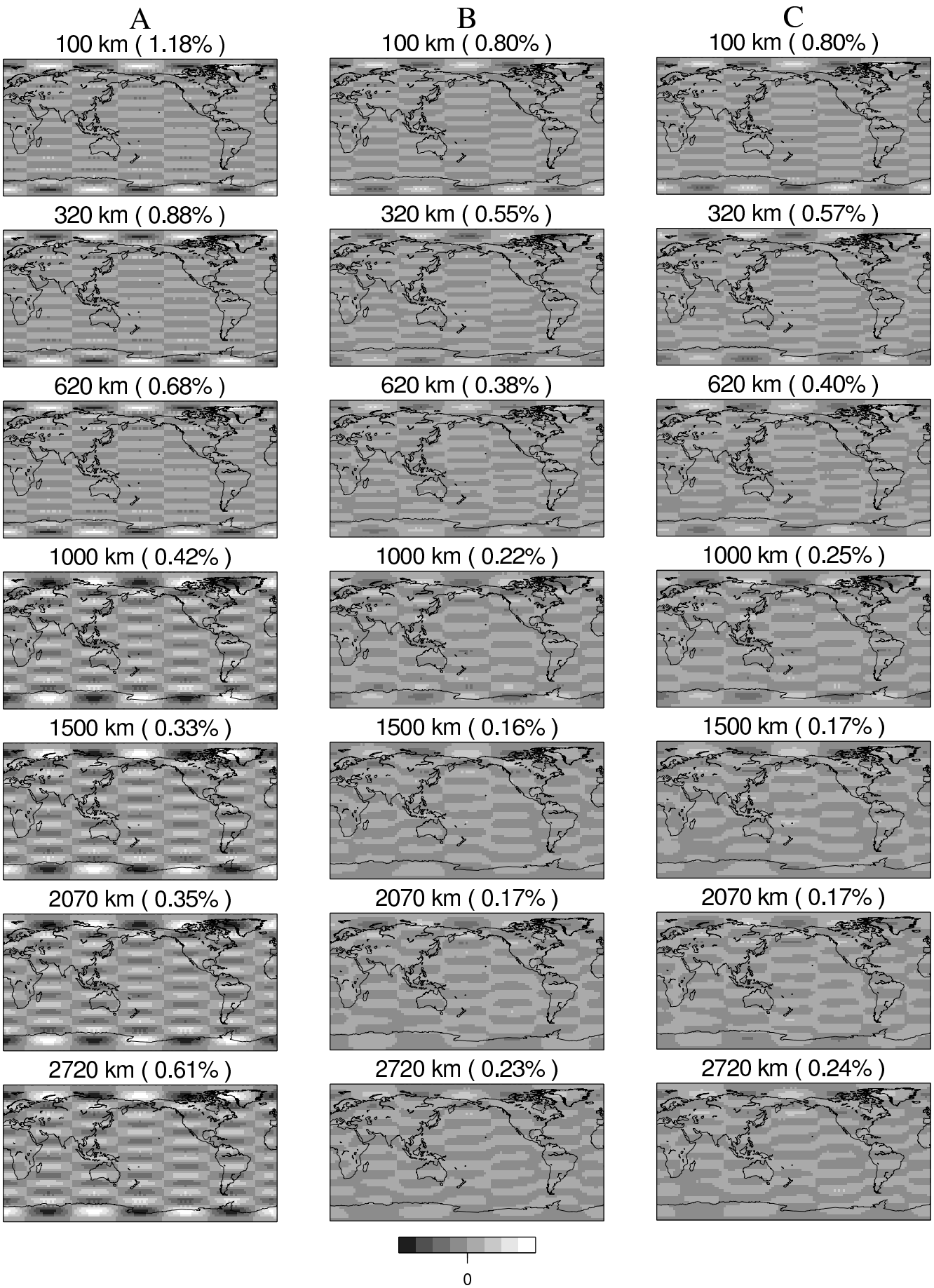
A
B
C
100 km (1.18%)
100 km (0.80%)
100 km (0.80%)
320 km (0.88%)
320 km (0.55%)
320 km (0.57%)
620 km (0.68%)
620 km (0.38%)
620 km (0.40%)
1000 km (0.42%)
1000 km (0.22%)
1000 km (0.25%)
1500 km (0.33%)
1500 km (0.16%)
1500 km (0.17%)
2070 km (0.35%)
2070 km (0.17%)
2070 km (0.17%)
2720 km (0.61%)
2720 km (0.23%)
2720 km (0.24%)
0

Figure 20

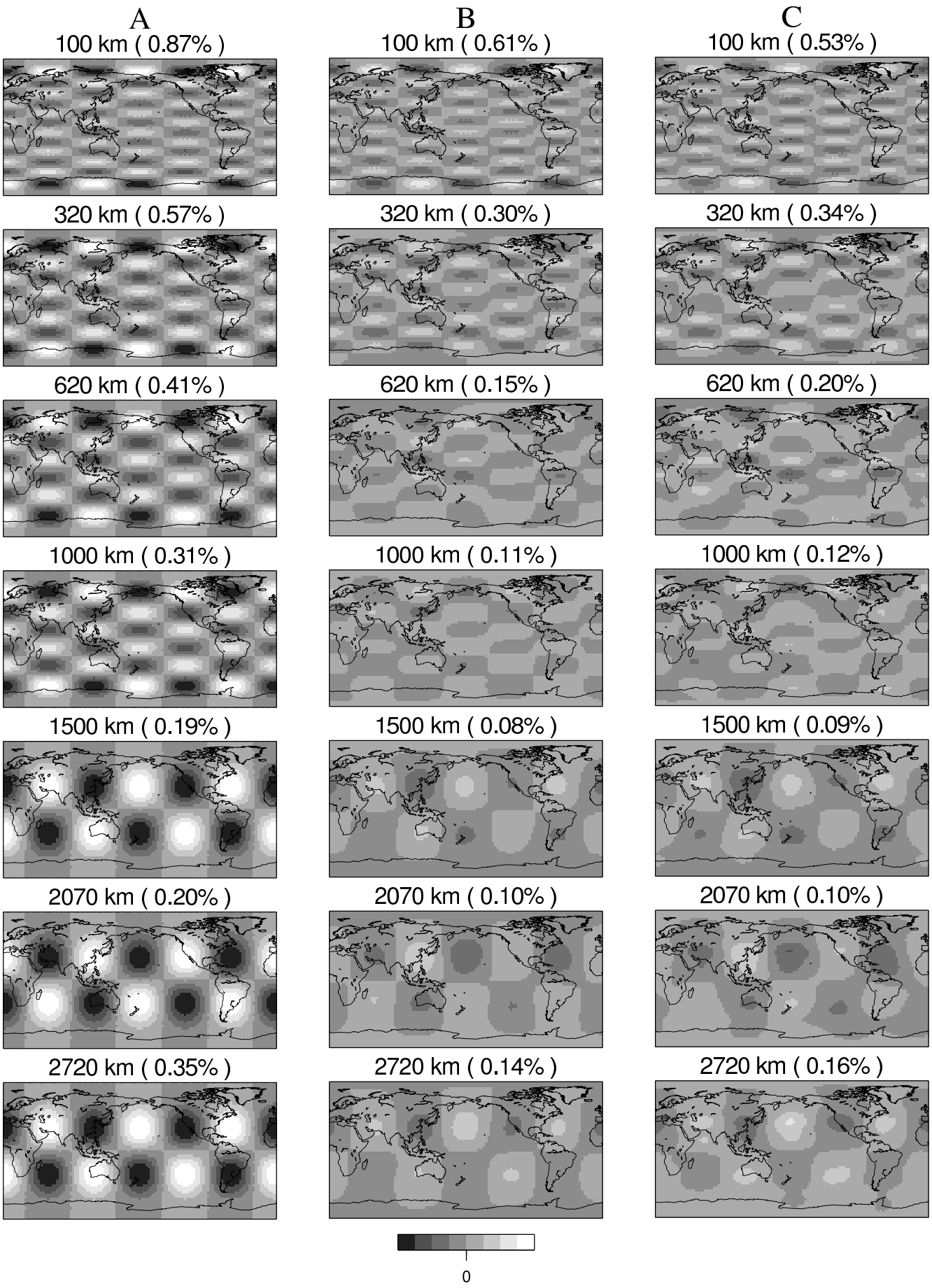
A
B
C
100 km (0.87%)
100 km (0.61%)
100 km (0.53%)
320 km (0.57%)
320 km (0.30%)
320 km (0.34%)
620 km (0.41%)
620 km (0.15%)
620 km (0.20%)
1000 km (0.31%)
1000 km (0.11%)
1000 km (0.12%)
1500 km (0.19%)
1500 km (0.08%)
1500 km (0.09%)
2070 km (0.20%)
2070 km (0.10%)
2070 km (0.10%)
2720 km (0.35%)
2720 km (0.14%)
2720 km (0.16%)
0

Figure 21

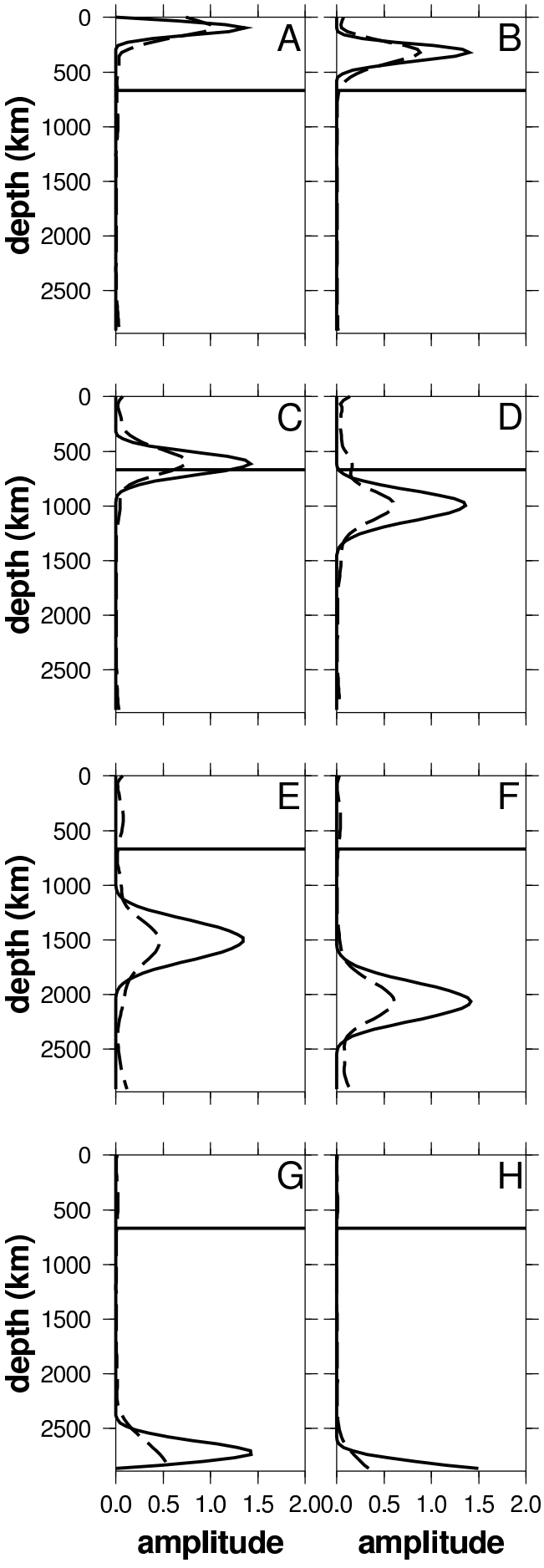
A
B
C
D
E
F
G
H
depth (km)
0
500
1000
1500
2000
2500
0.0 0.5 1.0 1.5 2.0
amplitude
0.0 0.5 1.0 1.5 2.0
amplitude

Figure 22

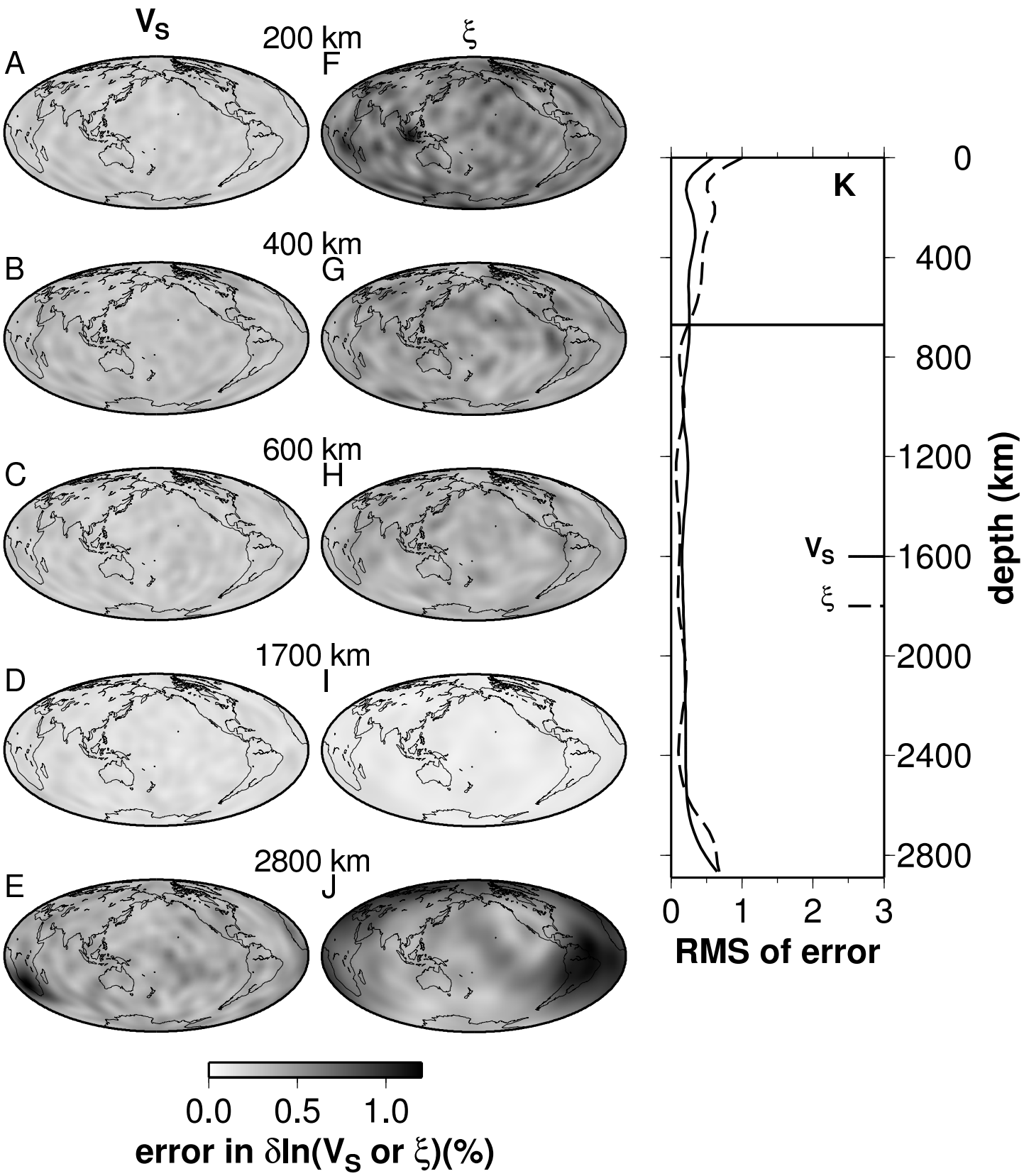
Vs
ξ
200 km
A
F
400 km
B
G
600 km
C
H
1700 km
D
I
2800 km
E
J
0.0
0.5
1.0
error in δln(Vs or ξ)(%)
K
Vs
ξ
0
400
800
1200
1600
2000
2400
2800
depth (km)
0
1
2
3
RMS of error

Figure 23

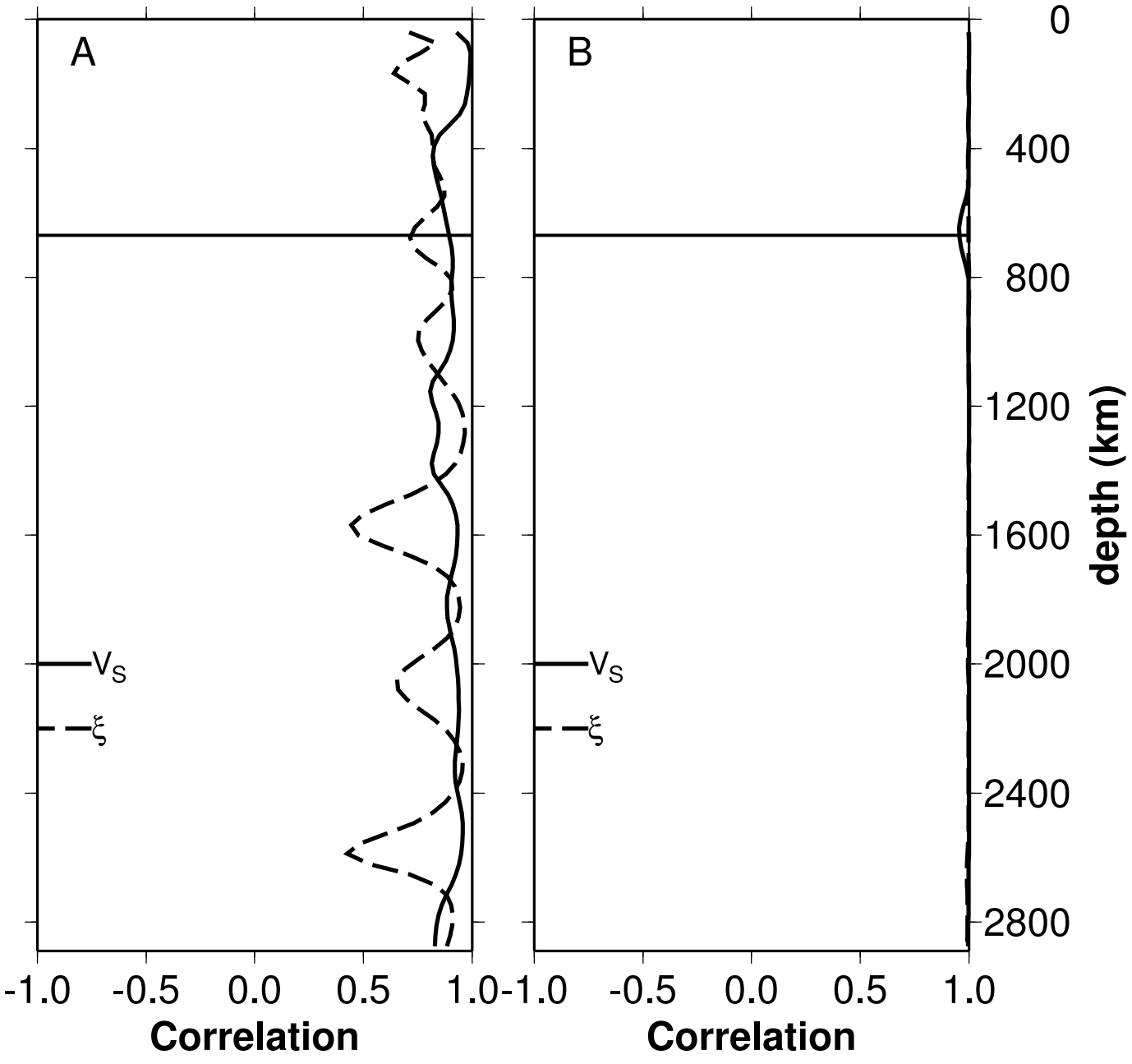
A
B
V_S
ξ
V_S
ξ
-1.0
-0.5
0.0
0.5
1.0
-1.0
-0.5
0.0
0.5
1.0
Correlation
Correlation
0
400
800
1200
1600
2000
2400
2800
depth (km)

Figure 24

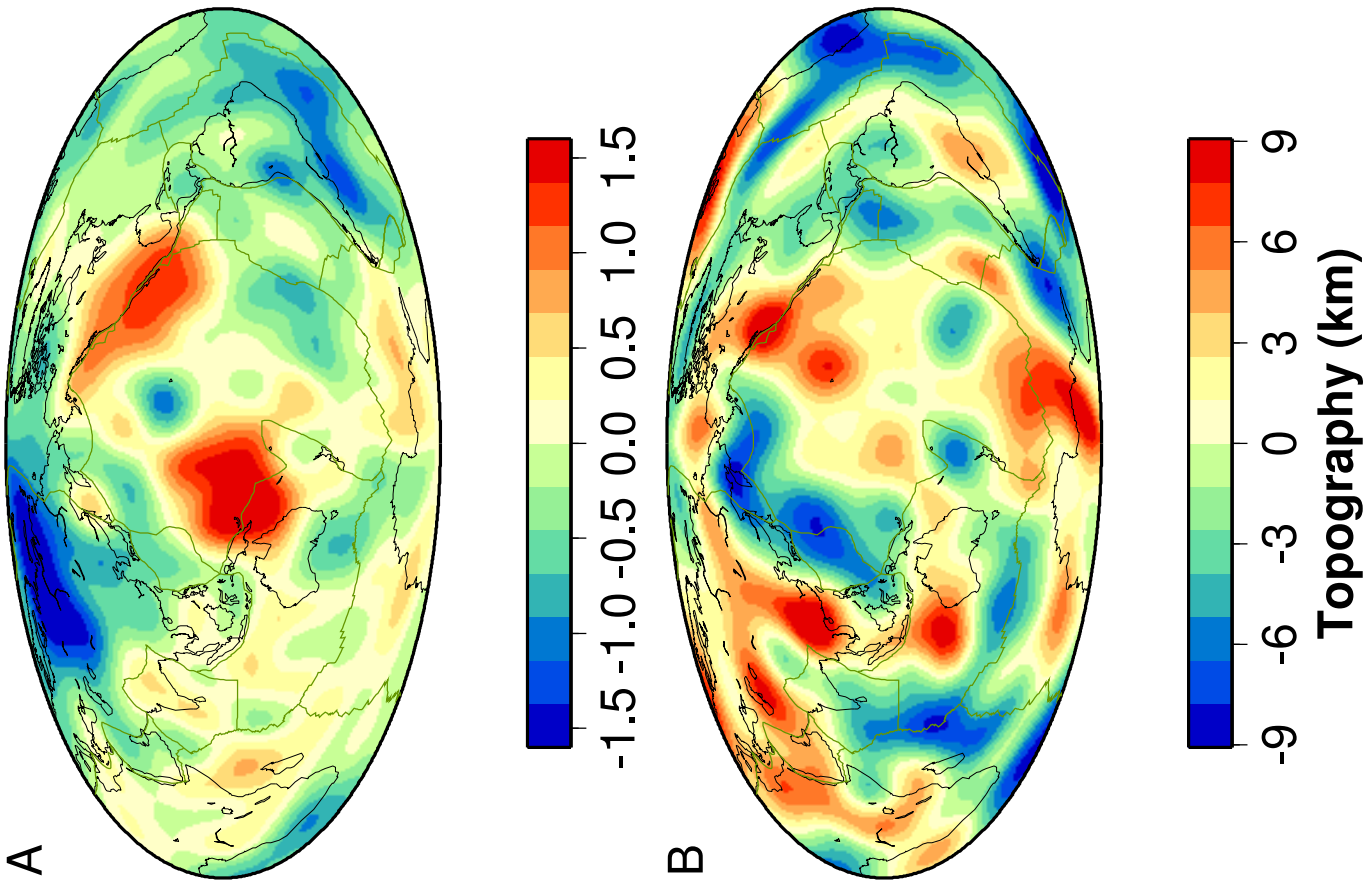

Figure 25

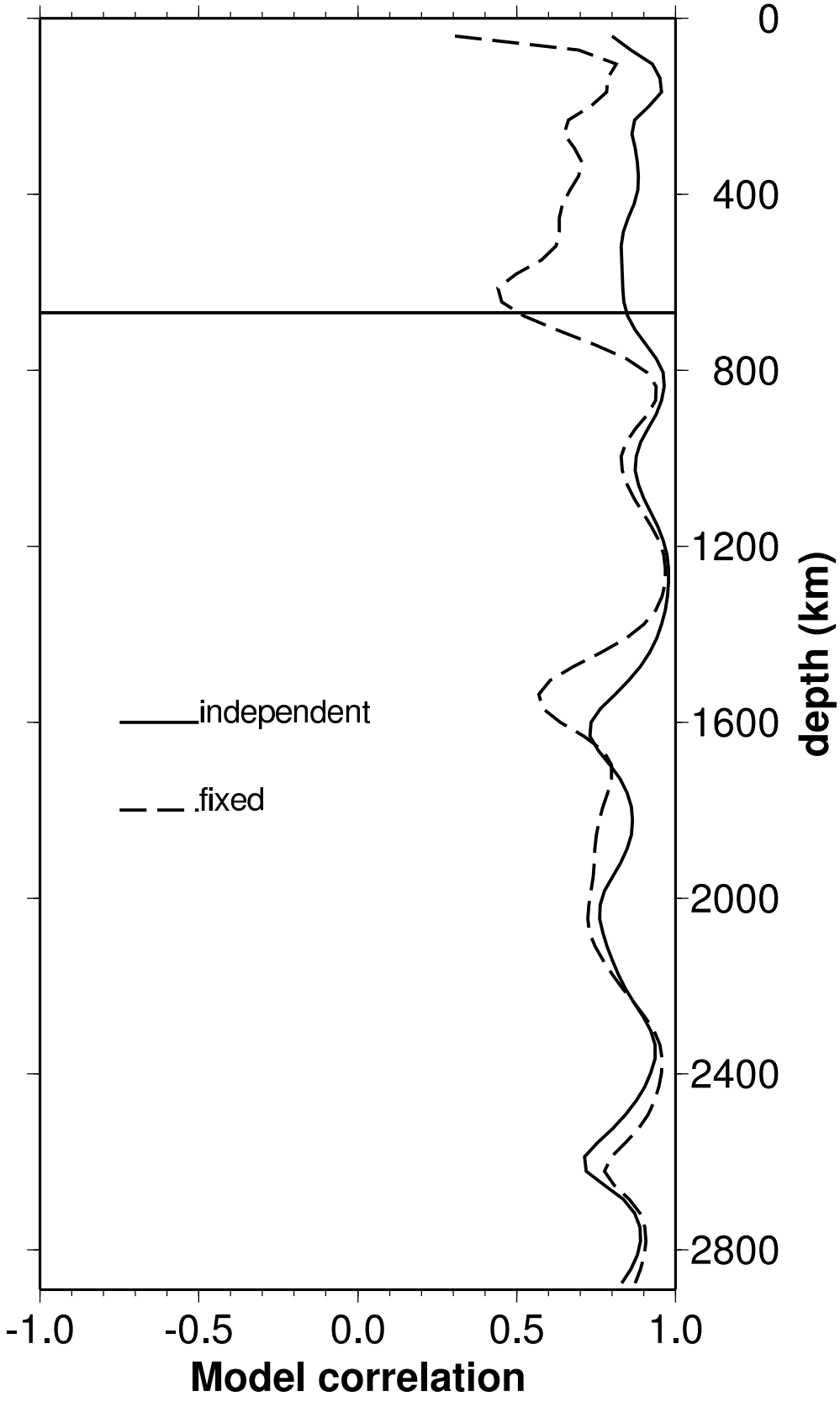
0
400
800
1200
1600
2000
2400
2800
depth (km)
independent
.fixed
-1.0
-0.5
0.0
0.5
1.0
Model correlation

Figure 26

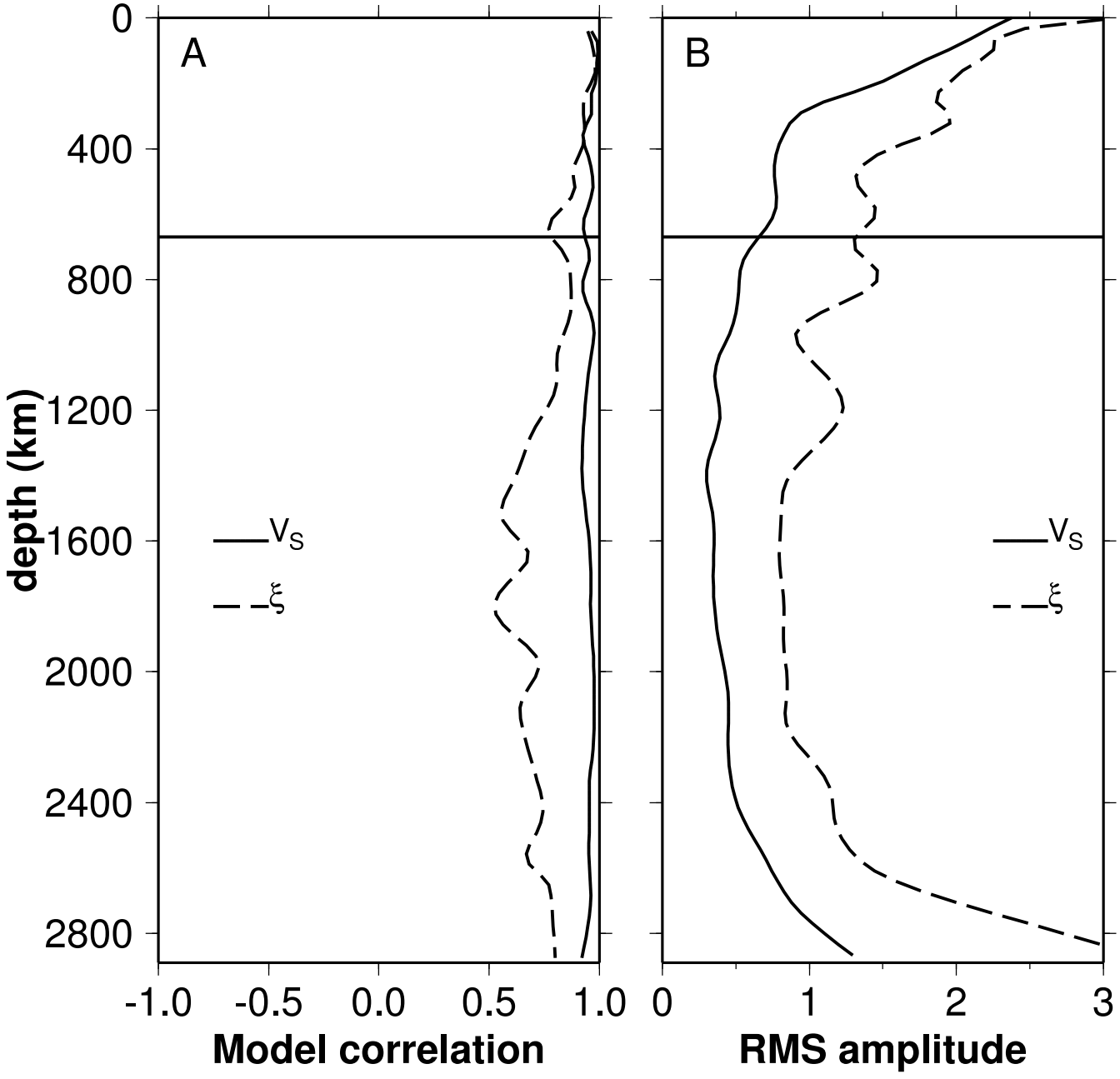
A
B
0
400
800
1200
1600
2000
2400
2800
depth (km)
V_S
ξ
-1.0
-0.5
0.0
0.5
1.0
Model correlation
0
1
2
3
RMS amplitude